Magnetic domain walls and domains in thin films, nano stripes and 3D structures

Dissertation zur Erlangung des Doktorgrades der Naturwissenschaften (Dr. rer. nat.) der Fakultät für Physik der Universität Regensburg

vorgelegt von
Benedikt Ezra Nathanael Boehm aus
Berlin

im Jahr 2017

Promotionsgesuch eingeleitet am: 12.07.2017
Die Arbeit wurde angeleitet von: Prof. Dr. Christian H. Back

Prüfungsausschuss:

Vorsitzender:	Prof. Dr. Ferdinand Evers
1. Gutachter:	Prof. Dr. Christian H. Back
2. Gutachter:	Prof. Dr. Jascha Repp
weiterer Prüfer:	Prof. Dr. Christoph Strunk

Das Promotionskolloquium fand statt am: 24.11.2017

Acknowledgements

First of all I would like to thank Rolf Allenspach, who always took the time to discuss not only physics but also everything else, who shared his knowledge about magnetism, helped me in the laboratory, carefully read my manuscript and kept as much administrative duties as possible away from me.

I am grateful to Christian Back especially for giving me the opportunity to work on my Ph.D., for his input to the experiments and for the secondment at the University of Regensburg.

A big thank you also goes to Andreas Bischof, who as a technician took care of the experimental set-up, continuously improved it and helped me with any technical challenge.

Thanks to André Bisig for the fruitful collaboration during his time as Post Doc. He developed the EBL process and shared his experience in the clean room as well as his experience in magnetism.

I am thankful to Leo Gross for explaining and helping me with the stencil set-up.

I would like to thank Peggy Schönherr for introducing me to the spin-SEM when I started at IBM.

Oliver Reich, who did his master's thesis at IBM acquired a lot of data on the Ni/Cu and Ni/Fe/Cu samples, while I was busy writing my thesis, thank you for that.

Thanks to Daniel Widmer for helping me with the VSM set-up.

I would like also to thank all colleagues, including the ones I already mentioned, for the friendly atmosphere and the great discussions, which makes IBM a pleasant place to work at.

Special thanks to Georgios Stefanou for the three weeks we shared at Leeds University in order to grow and characterise samples, but of course also for growing samples without my presence.

I also appreciate very much the opportunity for the secondment in the group of Bryan Hickey at Leeds University.

I am grateful also to all the members of the SPINICUR training network, for the good time, the fruitful discussions and exchange of knowledge during and between all the meetings we had.

Last but not least I would like to thank my whole family for always supporting me on the way to where I am now.

Contents

1 Overview

Ever since the first theoretical description of domains and domain walls by Weiss, more and more effort was put into this field of research. In the beginning, the formation of domains and domain walls on the surface of bulk materials was experimentally investigated and theoretical models developed. The two prototypical domain wall types, namely Bloch and Néel walls, were discovered and already interesting details were investigated, e.g., zigzag patterns in Bloch walls [1]. At about the same time an explanation for a small net ferromagnetic moment in some antiferromagnetic materials was developed: The Dzyaloshinskii–Moriya interaction [2, 3]. With the possibility to grow thin films more details about domains and their walls were revealed. For example at IBM Research – Zurich the transition from Néel to Bloch walls via cross-tie walls in in-plane magnetised materials was investigated on a wedge of NiFe [4]. Shortly after, models for the newly discovered physics were developed, e.g., a theory to explain the Néel – Bloch wall transition [5] and a theory about domain walls in the limit of one dimension [6]. With further improvements in the quality of thin films and especially measurement techniques earlier hidden features were discovered, as for example the Néel cap of Bloch domain walls in bulk materials [7]. Additionally, newly fabricated small magnetic structures, e.g., nanowires or nano stripes, showed several new domain wall types, e.g., vortex walls, anti-vortex walls, symmetric and asymmetric transverse walls, and allowed controlled displacements of domain walls along the wires by magnetic fields or spin-polarised currents. Also the wide accessibility of computers and free micromagnetic simulation software helped to understand the physics of domain walls. Recently the Dzyaloshinskii–Moriya interaction was rediscovered as its effect in thin films and small structures can be significant. For example, it changes the energetically preferred domain wall type and introduces a chirality for domain walls [8–11]. Such stabilised domain walls can have much higher wall velocities than without this interaction [12].

Still, the rich physics of domains and domain walls need yet to be fully understood. In this thesis we address this by imaging domains and domain walls by spin-polarised scanning electron microscopy in three different magnetic material systems. Spin-polarised scanning electron microscopy is a powerful technique for that purpose because it allows the direct probing of the magnetisation in a specimen with the spatial resolution of a scanning electron microscope which is around 10 nm in our system.

The following chapter is devoted to the basic theoretical background necessary to understand the experiments. A brief discussion about the spin-orbit interaction highlights the importance of this interaction for the field of magnetism. A section about domain walls reminds the reader about the domain wall types in perpendicularly magnetised materials. Finally the Dzyaloshinskii–Moriya interaction and its influence on domain walls are discussed.

Chapter 3 details the experimental set-up, in particular the spin-polarised scanning electron microscopy tool used for our experimental investigations. We look at how we measure the magnetisation of a specimen, in order to correctly interpret the recorded magnetic patterns. It turns out that it is often crucial to be capable to determine all three magnetization components. To this end, we have built a "spin rotator", i.e., an extension to the microscope which allows us to measure all three components of the magnetisation vector.

In the following chapter, differently arranged stacks of nickel and iron on top of the (100) surface of copper are investigated. The magnetic materials are evaporated in-situ onto the copper crystal which guarantees a high purity of the ferromagnetic materials. The domain walls in this system with perpendicular magnetisation are imaged and we find Néel, Bloch and intermediate domain walls. From the results we can conclude that the symmetry is broken in such a way that a chiral interaction is obtained, i.e., Dzyaloshinskii–Moriya interaction. We estimate the strength of this interaction and compare our results with literature values.

Chapter 5 deals with perpendicularly magnetised nanowires, which exhibit distinct domain wall types depending on the geometry. Nanowires with different width are shaped out of a sputtered cobalt/nickel multilayer by an electron beam lithography process. The transition of the domain wall type in the nanowires is investigated by direct imaging of the wall structure. We discover an achiral intermediate wall type that is unpredicted by established theoretical models. With the help of micromagnetic simulations, the formation of this novel wall type is explained. We discuss why this intermediate wall should occur in all perpendicularly magnetised materials for appropriate wire dimensions and we exclude Dzyaloshinskii–Moriya interaction as a possible cause for this novel wall type.

Finally, in chapter 6, three-dimensional magnetic cobalt structures are investigated, which are the first step towards three-dimensional, extended, magnetic spin ice networks. We show that two-photon lithography in combination with electroplating is capable of producing large arrays of three dimensional magnetic structures in the submicrometre range by imaging the domain pattern in these structures. Additionally, we show how a detailed analysis by spin-polarised scanning electron microscopy can be used to improve the production process of samples.

2 Background

2.1 Spin-Orbit Interaction

One of the most famous examples of spin-orbit interaction is the fine structure, i.e. a splitting in the energy levels of the atomic shells which was discovered by the splitting of spectral lines in the optical emission spectra of alkali metals in the first quarter of the 20th century. As the name suggest the spin-orbit interaction couples the electron spin angular momentum $\boldsymbol{S}$ to its orbital angular momentum $\boldsymbol{L}$, which are merged to a combined quantum number: The total angular momentum $\boldsymbol{J}$. Spin-orbit coupling can be derived from the Dirac equation (without any additional assumptions) [13]. The Hamiltonian of the spin-orbit interaction is defined as [14, 15]

$$\mathcal{H} = \xi \, \boldsymbol{S} \cdot \boldsymbol{L} \tag{2.1}$$

where ξ is called spin-orbit parameter or coupling constant. The coupling constant depends strongly on the radius of the atomic shell, the atomic number Z and which electrons are considered, e.g., when considering only the outer shells the parameter increases with Z^4 for elements with the 3d shell being the most outer one, while in average over all elements it increases with Z^2 [15].

Additionally to the fine structure the spin-orbit interaction is responsible for several phenomenon. For this work very important is the scattering of electrons at nuclei. The differential scattering cross section of an electron beam with polarisation $\boldsymbol{P}$ is given by [13]

$$\sigma = I \left(1 + S\boldsymbol{P} \cdot \hat{\boldsymbol{n}}\right), \tag{2.2}$$

where I is the scattering amplitude, S the Sherman function and $\hat{\boldsymbol{n}}$ the unit vector perpendicular to the scattering plane. We will discuss this so called "Mott scattering" in a semi-classical picture in subsection 3.2.1. However, we can already draw important conclusions from this formula: First of all the scattering is spin dependent, and second only electrons with polarisation vector components perpendicular to the scattering plane get scattered in this plane, therefore only two components of the polarisation vector can be scattered in one plane.

The spin-orbit interaction plays also an essential role in magnetism. For example, since the scalar product in Equation 2.1 vanishes for a parallel alignment of spin and angular momentum, one can easily see that this is the preferred state. In magnetic crystals where the orbital moment prefers to lie along a specific lattice direction this gives rise to the magnetocrystalline anisotropy energy.

2.2 Domain Walls

The formation of domains results from the interplay of the anisotropy and the demagnetisation energy (also called shape anisotropy). In a ferromagnet the anisotropy energy is minimal when the magnet is magnetised homogeneously, however, this creates strong fringing fields. These fields can be kept small by the formation of magnetic domains with the magnetisation pointing in different directions. The transition from one domain to another happens continuously and is called a domain wall. In ferromagnetic materials two prototypical domain wall types exist: The magnetisation can either rotate perpendicularly to the domain wall cross-section, i.e., a Bloch wall, or in the cross-section, i.e., a Néel domain wall, as sketched in Figure 2.1 for a perpendicularly magnetised material. Throughout this work the coordinate system for domain walls will be the same, if not

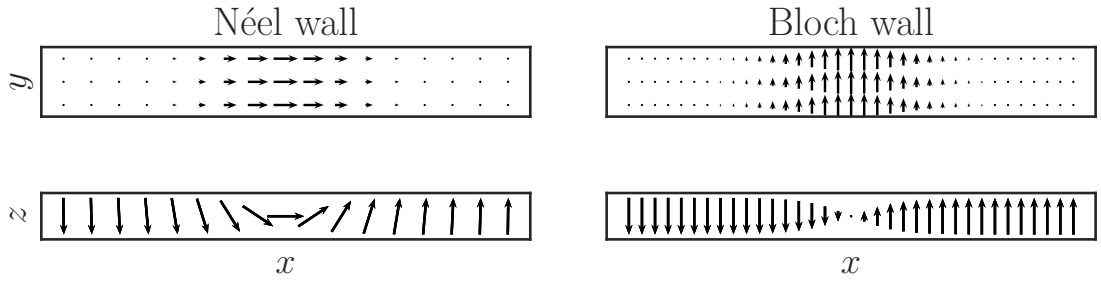

Figure 2.1: Sketch of the two prototypical domain wall types in perpendicularly magnetised materials, with arrows representing the magnetic moments. The upper sketches picture the magnetisation in the xy-plane, i.e., the view from the top. The bottom ones show the magnetisation in the xz-plane, i.e., the cross-section of the wall. The magnetisation in a Néel wall rotates in the xz-plane, while the magnetisation in a Bloch wall rotates in the yz-plane.

otherwise stated, i.e., the cross-section of a domain wall will be the xz-plane and the magnetisation of a Bloch wall will point along the y-direction.

The rotation can also happen as a combination of the two prototypical types: A "intermediate" domain wall as shown in Figure 2.2. For the purpose of classifying the walls we introduce the azimuthal (in-plane) angle ψ (magnetic moment angle) of the wall, which we define by $\tan(\psi) = m_y/m_x$, where $m_{x,y,z}$ are the components of the reduced magnetisation $\boldsymbol{m} = (m_x, m_y, m_z) = \boldsymbol{M}/|\boldsymbol{M}|$. Therefore we have Néel walls for $\psi = 0$ or 180°, Bloch walls for 90 or 270°, and intermediate domain walls for all other angles. Because it is unambiguous we mention the "Bloch" (Néel) component of a wall when talking about m_y (m_x). When a wall has a Néel component we can define a chirality, i.e., an unambiguous classification of the rotation direction. We define the chirality of a wall with the in-plane magnetisation direction pointing towards a domain with negative z-component as right-handed. For example the Néel wall in Figure 2.1 shows a left-handed chirality, while the intermediate wall in Figure 2.2 shows a right-handed one.

The width d_w of a domain wall is given by the equilibrium between exchange and magnetocrystalline anisotropy. In the one-dimensional (1D) model the energy associated

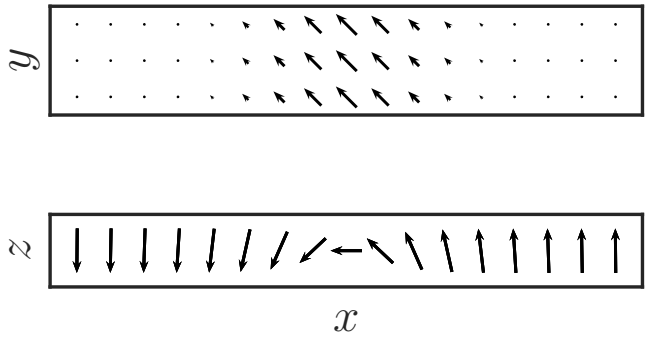

Figure 2.2: Sketch of a intermediate domain wall.

with the formation of a Bloch wall with a gradual changing magnetisation in an infinite extended perpendicularly magnetised film is [16]

$$E_w = 4\sqrt{AK_u}, \tag{2.3}$$

where A is the exchange constant and K_u the magnetocrystalline anisotropy constant. The energy is minimal for a domain wall width

$$d_w = \pi\sqrt{A/K_u}. \tag{2.4}$$

When we want to determine the energy of also Néel and intermediate domain walls we need to take into account the shape anisotropy, which is lower in the case of a Bloch wall compared to a Néel wall. Therefore, the energy difference σ which is caused by the magnetostatic shape anisotropy K_s of the wall depends on ψ. We assume that the domain wall width d_w is independent of the wall type. Additionally, we replace the exchange stiffness A with an expression derived from Equation 2.4 and assume that the magnetic material thickness t is small compared to the characteristic length of the exchange interaction [17], which is equal to the (reduced) domain wall width $\Delta = d_w/\pi$. Thus the energy difference is [9]

$$\sigma = \frac{2d_w K_s}{\pi}\cos^2(\psi) = 2\Delta K_s \cos^2(\psi), \tag{2.5}$$

where $K_s = N_x\mu_0 M_s^2/2$ with $N_x = t\ln(2)/d_w$ being the demagnetisation coefficient of the wall [17].

In our experiments we measure the components of the reduced magnetisation. The components of the profile of a domain wall in a perpendicularly magnetised material is

in the 1D model [18]:

$$\begin{aligned} m_x(x) &= \cos(\psi)/\cosh\left(\frac{x-x_0}{\Delta}\right), \\ m_y(x) &= \sin(\psi)/\cosh\left(\frac{x-x_0}{\Delta}\right), \\ m_z(x) &= \tanh\left(\frac{x-x_0}{\Delta}\right), \end{aligned} \tag{2.6}$$

where x_0 is the centre of the wall. With this domain wall profile we fit our measurements to determine the domain wall width Δ and the azimuthal angle ψ.

2.3 Dzyaloshinskii–Moriya Interaction

In the middle of the 20th century researchers found an interesting behaviour in Fe_2O_3 [19], $MnCO_3$ and $CoCO_3$ [20]: These materials are antiferromagnetic, however, a weak ferromagnetic component can be detected. This provoked Dzyaloshinskii [2] to come up with a phenomenological explanation based on the symmetry breaking in the crystal, which favours a small canting of the magnetic moments, which in turn results in weak ferromagnetism. Moriya [3] picked this up shortly after and developed a quantum-mechanical theory, which led to the name Dzyaloshinskii–Moriya interaction (DMI). It is an exchange interaction based on spin-orbit interaction, which, following the rules of Moriya, only appears in materials with a non-centrosymmetric structure. Therefore DMI is also referred to as antisymmetric exchange interaction [14]. In order for DMI to arise, the symmetry of a system has to be broken. Crystals are usually highly ordered and structured and therefore a symmetry breaking in the bulk seems unreasonable. However, the examples Fe_2O_3, $MnCO_3$ and $CoCO_3$ show, indeed, that DMI can origin from symmetry breaking in bulk crystals. For example in Fe_2O_3 the spins slightly tilt out of the (111) plane, making an angle of 10^{-4} rad with the plane. The tilting results in a spontaneous magnetic moment of 0.04 % of the nominal value [2].

An appearance of DMI in centrosymmetric crystals is also possible due to, for example, stress or applied magnetic or electric fields. However, the resulting chiral magnetic couplings could be very weak in bulk materials [21]. Especially pseudomorphically grown materials with a strain gradient are predestined for a bulk DMI, as the inhomogeneous stress gets released by misfit dislocations, creating a symmetry breaking at each layer. A theoretical investigation of three differently strained layers of body centred cubic (bcc) iron (Fe), indeed, showed the appearance of DMI in this system [22].

The symmetry breaking can, for example, also take place at the interface to a non-magnetic material. Fert *et al.* [23] investigated this with their so called "3-site mechanism", which considers the interaction of two nearest neighbour magnetic moments with an adjacent non-magnetic atom. It is not only restricted to interfaces, for example it can also be applied to a magnetic material which is doped with non-magnetic atoms.

In general, the energy associated with Dzyaloshinskii–Moriya interaction of two spins

$\boldsymbol{S}_i$ and $\boldsymbol{S}_j$ for the atomic bond ij can be expressed as follows

$$E_{ij} = \boldsymbol{d}_{ij} \cdot (\boldsymbol{S}_i \times \boldsymbol{S}_j)\,, \tag{2.7}$$

where $\boldsymbol{d}_{ij}$ is the DMI vector [24]. Because of its antisymmetric nature the DMI constant changes sign for a commutation of $\boldsymbol{S}_i$ and $\boldsymbol{S}_j$.

In a film where the DMI is created at the interface of the magnetic and adjacent layer the DMI vector can be expressed as $u_{ij} \times \hat{z}$, where u_{ij} is the unit vector pointing from site i to site j and $\hat{z}$ is the direction normal to the film. The DMI vector therefore lies in the plane, favouring one in-plane magnetisation direction. A direct consequence of Equation 2.7 is a canting of adjacent magnetic moments. Whether the direction of the canting of the two spins is towards or away from each other depends on the relative direction of $\boldsymbol{d}_{ij}$ and $\boldsymbol{S}_i \times \boldsymbol{S}_j$. This results in a given rotation sense for a system – a chirality is introduced. In perpendicularly magnetised systems a sufficiently strong DMI results in the appearance of pure Néel domain walls, for weaker DMI intermediate domain walls appear. In order to estimate the DMI we average the DMI vector over the whole sample and get an effective DMI constant D. Note that when D is given with a negative value it indicates pointing in the opposite direction. With this simplification we can add a DMI term to the domain wall energy of (Equation 2.5) [9]:

$$\sigma = 2\Delta K_s \cos^2(\psi) - \pi D \cos(\psi)\,. \tag{2.8}$$

In order to find the azimuthal angle for a given D we need to minimise the energy with respect to ψ, which results in the static solution [9]

$$\begin{aligned} \cos(\psi) &= \frac{\pi D}{4\Delta K_s} \text{ for } \pi|D| \leq 4\Delta K_s \\ &= \operatorname{sign}(D) \text{ for } \pi|D| > 4\Delta K_s. \end{aligned} \tag{2.9}$$

As shown in Figure 2.3, in infinitely extended perpendicularly magnetised films without DMI the preferred domain wall type is a Bloch domain wall. By introducing DMI the magnetic moment in the wall starts to rotate towards the Néel configuration. This transition happens gradually and stops at a critical value

$$D_c = 4\Delta K_s/\pi, \tag{2.10}$$

after which the domain wall does not change further. If we include the formulas for K_s and N_x in Equation 2.10, we get an equation which is independent on the domain wall width:

$$D_c = \frac{4\Delta t \ln(2)\mu_0 M_s^2}{2\pi^2\Delta} = \frac{2t\ln(2)\mu_0 M_s^2}{\pi^2} \tag{2.11}$$

Modifications of the domain wall energy also causes other effects: Earlier it was found that the width of domains depends on the domain wall energy [25–27]. The DMI, therefore, also alters the size of the domains in a given system. The domain width W can be approximated as follows [27]:

$$W = xt \exp\left(\frac{\sigma}{\mu_0 M_s^2}\right), \tag{2.12}$$

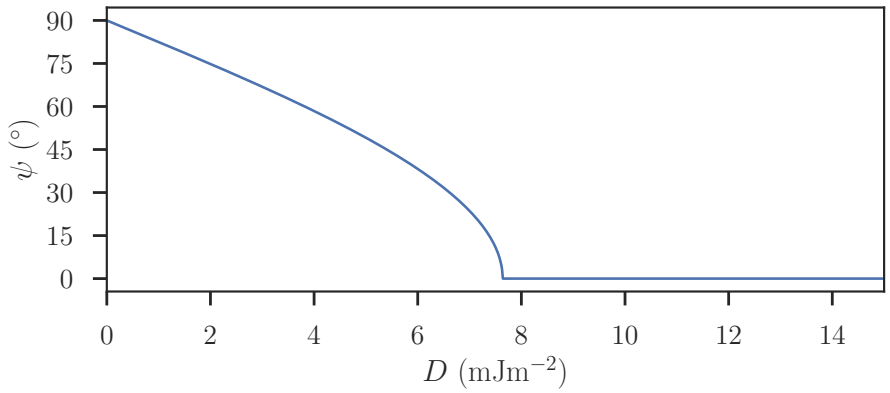

Figure 2.3: The magnetic moment angle ψ versus the DMI constant for a domain wall width $\Delta = 10\,\mathrm{nm}$ and a magnetostatic shape anisotropy $K_s = 600\,\mathrm{kJ\,m^{-3}}$ calculated with Equation 2.9.

where x is a factor depending on the domain structure. For stripe domains it has the value $x = 0.955$.

3 Spin-Polarised Scanning Electron Microscopy

The first utilization of electrons to overcome the resolution limits of light imaging techniques was achieved in 1931 with a transmission electron microscope (TEM) [28]. A TEM uses a focused electron beam to scan over a sample while the electrons transmitted are detected. The electrons interact with the material they pass through and therefore the intensity of the electron beam depends on the topography and material composition of the specimen's surface. The same is true for reflected electrons, which was experimentally demonstrated shortly after [29]. This was the starting point for the development of scanning electron microscopy (SEMs). However, it took more than 30 years until technical advances allowed a resolution of about 10 nm to be achieved [30]. Even though spin dependent scattering of electrons on a nucleus was already discussed in 1929 by Mott [31], in 1984 the fist time a so called "Mott analyser" was used as detector in an SEM to analyse the electron spin [32]. This combination is nowadays referred to as a spin-polarised scanning electron microscope (spin-SEM) [33] or scanning electron microscope with polarisation analysis (SEMPA) [34].

3.1 Scanning Electron Microscopy

In a SEM an electron beam is scanned over the surface of a sample. The signal acquired in various detectors is then mapped to the beam position, in this way micrographs are constructed. In our ultra-high vacuum (UHV) system we use a "UHV Gemini Electron Column" to create the electron beam. When the beam of electrons (so called primary electrons) hit the specimen they can interact with the coulomb field of the electrons and nuclei of the specimen, resulting in elastic and inelastic scattering. This interaction is the origin of multiple signal sources, e.g. secondary electrons, back-scattered electrons, Auger electrons and x-rays. Electrons which get absorbed by the specimen can be measured as "absorbed" current, which yields another signal source. The absorbed current is highly sensitive to changes in the chemical potential and therefore ideal to identify different materials. In our set-up we make use of the absorbed current and the secondary electrons, which are electrons which were expelled by inelastic scattering with a primary electron.

3.2 Mott Analyser

Electrons carry the information of the specimen's magnetisation in its spin: Their magnetic moment is

$$\boldsymbol{m} = -\frac{g\mu_B}{\hbar}\boldsymbol{S}, \tag{3.1}$$

where g is the g-factor, μ_B the Bohr magneton and $\hbar$ the reduced Planck constant. When the electrons of the 3d subshell, which carry the magnetisation information, leave the sample they keep their spin orientation. In metals the mean free path of electrons is 1 nm [35]. Therefore only secondary electrons created in the top view monolayers of the specimen can escape. Thus, if we can analyse the polarisation of these electrons we know the magnetisation at the sample's surface. For the purpose of separating electrons depending on their spin, Mott [31] discussed scattering them on the nucleus' Coulomb field of heavy atoms. This spin-obit interaction based process is nowadays referred to as "Mott scattering", and is used in so called "Mott analysers". For the purpose of scattering the secondary electrons get focused by electron optics to form an electron beam, whose spin polarisation as well as intensity depend strongly on the secondary electron's energy as shown in Figure 3.1.

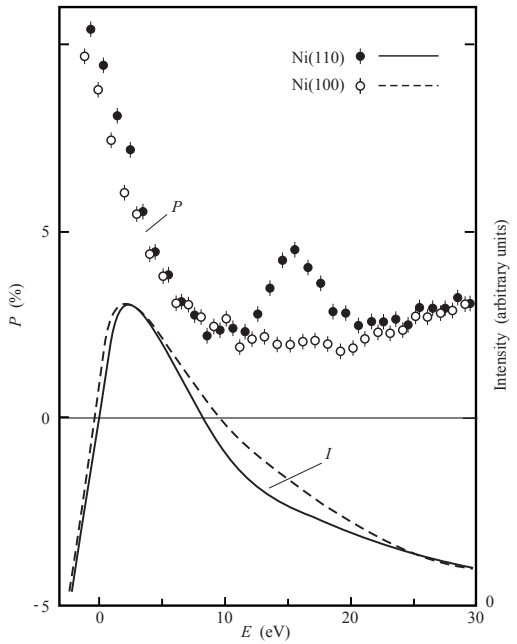

Figure 3.1: The intensity and polarisation of secondary electrons created at the surface of Ni(100) and Ni(110) versus their kinetic energy, recorded at a primary-electron energy of 600 eV. Figure from [36].

3.2.1 Principle and Geometry

The secondary electrons get accelerated towards a thin foil of heavy atoms such as gold. Because of its high energy the electrons penetrate deep into the Coulomb field of the atoms and interact with their nuclei. In a semi-classical picture the positively charged nucleus moves in the rest frame of the electron towards the electron, creating a circular inhomogeneous magnetic field, which gets stronger towards the core [35]. The energy E of a magnetic moment $\boldsymbol{\mu}$ in a magnetic field $\boldsymbol{H}$ is $E = -\boldsymbol{\mu} \cdot \boldsymbol{H}$, thus the force the field applies to the moment is given by the negative gradient of the energy:

$$\boldsymbol{F} = \nabla (\boldsymbol{\mu} \cdot \boldsymbol{H}) \tag{3.2}$$

An electron with magnetic moment down (spin up) passing the nucleus on the right-hand side will have its moment aligned antiparallel to the field, and therefore will get pushed towards decreasing fields, i. e. the right-hand side. If the electron passes on the left-hand side, magnetic moment and magnetic field will be parallel and the electron will get pushed towards increasing fields, which is also the right-hand side. Therefore electrons with magnetic moment down get deflected to the right-hand side. Correspondingly, electrons with magnetic moments up will get pushed to the left, thus separating spin up and down electrons [35]. The electron beam is not only carrying the information of up and down magnetisation, but the correct orientation of the magnetisation in three dimensions. In our semiclassical model one component of the magnetic moment is aligned perpendicular to the magnetic field lines of the moving nucleus, thus the force vanished because the scalar product in Equation 3.2 vanishes, therefore only two components of the magnetisation can be analysed simultaneously. In a quantum-mechanical point of view the scattering process is based on spin-orbit interaction. One then investigates the scattering in a scattering plane, in which one is also limited to scatting of two components. In our system we use a gold foil to scatter the electrons. We detect the back scattered electrons with detectors every 90°. Thus allowing us to determine two of the three vector components of the magnetisation. We have set up our system so that we can detect the out-of-plane and one in-plane magnetisation component. By rotating the sample by 90° around the surface normal or by rotating the electron spin in a controlled way with a so called “spin rotator” we then can address the second in-plane component if needed.

3.2.2 Signal Processing

The spin polarisation P of an electron beam is defined as

$$P = \frac{n_\uparrow - n_\downarrow}{n_\uparrow + n_\downarrow}, \tag{3.3}$$

where $n_\uparrow$ and $n_\downarrow$ are the number of spin up and spin down electrons, respectively. In practice a lot more needs to be taken into account. The two biggest sources of a falsified spin polarisation are a beam which does not hit the gold foil perfectly perpendicularly,

and a beam which does not hit the foil in the centre of the four detectors. Therefore one usually measures in the detectors the left-right scattering asymmetry

$$A = \frac{N_L - N_R}{N_L + N_R}, \tag{3.4}$$

where N_L and N_R are the number of electrons scattered to the left and right side, respectively. The spin polarisation can then be determined with a so called effective Sherman function S

$$P = \frac{A}{S}. \tag{3.5}$$

This function has to be determined for each Mott detector. There are several methods of doing so, for example by measuring an electron beam with known polarisation [37]. This has been widely discussed in literature, therefore I may refer the reader to [13, 37–39]. Since we usually measure at least two domains with opposite magnetisation direction ($P \to -P = P'$) we can simplify the calculation and at the end the polarisation is given by

$$P = \frac{1}{S}\left(\frac{X-1}{X+1}\right), \tag{3.6}$$

where $X = \sqrt{N_L N'_R / N_R N'_L}$ and N and N' are the number of detected electrons in the corresponding detector (left or right) for two domains with opposite magnetisation [38]. Examples of a spin-polarised micrographs are shown in Figure 3.2. A positive

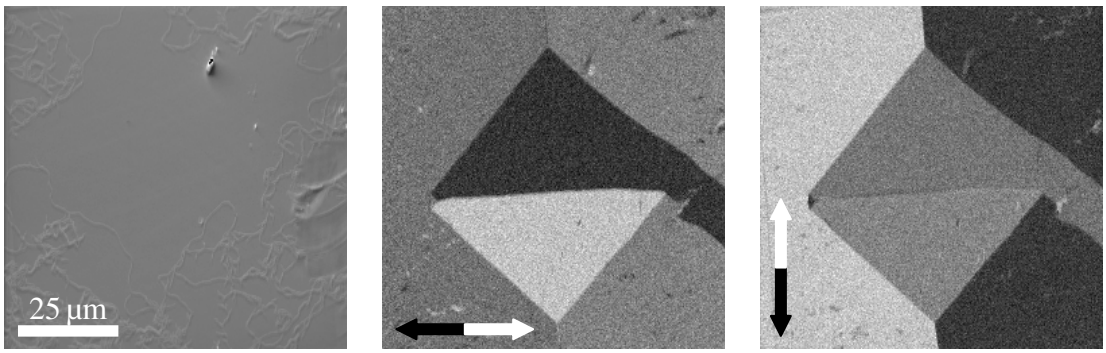

Figure 3.2: Intensity and spin-polarised micrographs of the surface of an Fe whisker. The image on the left-hand side shows the sum of all detectors in the Mott analyser, which is effectively the intensity of the electron beam arriving at the Mott detector, while the others show the polarisation determined by the corresponding detector pairs. The magnetisation (spin) direction is displayed in a right-handed coordinate system, with white (black) representing the positive direction, which is indicated by the arrow for the magnetisation. The spin polarisation – also called magnetic contrast – is 15 % (−15 %) for the white (black) area.

(negative) spin polarisation in a right-handed coordinate system is indicated by black

(white) regions. We decided to indicate the magnetisation direction with arrows for each polarisation direction. The same coding is used throughout the whole thesis. The polarisation in Figure 3.2 is 15 % (−15 %) for the white (black) area. When talking about images we also refer to the polarisation as magnetic contrast.

3.3 Spin Rotator

Besides the low efficiency of Mott detectors - approximately only every thousandth electron gets scattered into the backward direction [13] - also the detection of only two components of the magnetisation vector can be a problem. For example if magnetic structures should be investigated which have magnetisation components in all directions or if only one of the two important spin directions can be addressed simultaneously. Particularly in our set-up samples with only in-plane components required to be measured twice, the second measurement could be only done after a mechanical rotation of the sample. A mechanical rotation of the sample can be problematic, because it introduces mechanical drift, which fades only with time. Additionally when measuring with high magnification on thin films, the topography does not allow for easily finding the same spot again. However, acquiring all three magnetisation components, without a mechanical rotation can be achieved either with a second Mott analyser or a so called spin rotator [40–42].

3.3.1 Principle and Simulation

A spin rotator works after the principle of a Wien filter with crossed electric and magnetic fields. It rotates the electron's spin without deflecting the electron path. The magnetic field is used to rotate the spin of the electron due to Larmor precession. The principle is sketched in Figure 3.3. The rotation angle α can be calculated as follows [40]

$$\alpha = \frac{leB}{m_e v}, \tag{3.7}$$

where l is the distance the electron travels through the magnetic field, e the electron charge, B the absolute value of the magnetic induction $\boldsymbol{B}$, m_e the electron mass and v the velocity of the electron. Since the electron is a charged particle it gets deflected in the magnetic field by the Lorentz force

$$\boldsymbol{F}_L = -e\boldsymbol{v} \times \boldsymbol{B}. \tag{3.8}$$

Since the path of the electrons should not be altered an electric field $\boldsymbol{E}$ is used to counteract the magnetic induction. This means the total Lorentz force has to vanish:

$$\boldsymbol{F}_L = -e\left(\boldsymbol{E} + \boldsymbol{v} \times \boldsymbol{B}\right) \stackrel{!}{=} 0 \tag{3.9}$$

This yields for the electric Field

$$\boldsymbol{E} = -\boldsymbol{v} \times \boldsymbol{B}. \tag{3.10}$$

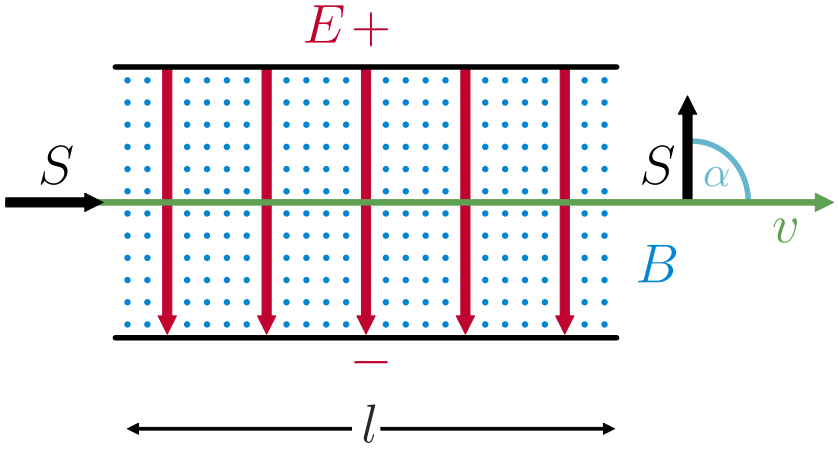

Figure 3.3: The principle of the spin rotator. An electron with spin $\boldsymbol{S}$ and velocity $\boldsymbol{v}$ passed through a magnetic field $\boldsymbol{B}$ of length l. The electron spin gets rotated due to Larmor precession. An electric field $\boldsymbol{E}$ is used to compensate the deflection of the electrons by the magnetic field. At the exit the electron leaves the spin rotator with a spin rotated by an angle of α.

Thus in order to compensate the effect of the magnetic and electric field on the electron path they must be perpendicular to each other and of the right strength. Even though the principle is rather simple designing a spin rotator is challenging, because at the entrance and exit of the spin rotator fringing fields exist. These fringing fields can change the spin and momentum of the electrons. For this purpose Kohashi *et al.* used electrodes with a "hyperbolically curved surfaces" and tapered edges, "which creates an ideal electric field for a stigmatic focusing effect" [41]. Their spin rotator was design to be 80 mm × 80 mm × 80 mm in size, in our system however there was not enough space for a spin rotator of these dimensions, therefore we adapted the design and shrunk it to 50 mm × 50 mm × 50 mm. We simulated an electron beam passing through the new design with the simulation software SIMION [43]. The simulation showed that it is possible to reduce the dimensions without losing the focusing effect as shown in Figure 3.4.

3.3.2 Calibration

After completely assembling the spin rotator, the strength of the magnetic induction in the middle between the two coils was tested. Therefore a Hall probe was fixed in the middle and a current through the coils was applied and measured. Fitting the data yields a slope of

$$B/I = 5.14\,\mathrm{mT\,A^{-1}}, \tag{3.11}$$

where $B = |\boldsymbol{B}|$. From our simulations we expect to need around 6 mT for a 90° rotation of the electron spin, which results in a calculated $I = 1.17\,\mathrm{A}$.

The spin rotator was inserted just in front of the Mott analyser. We oriented the

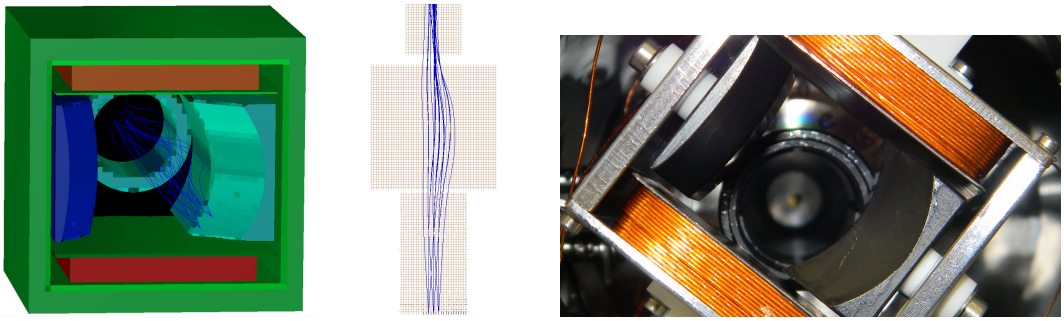

Figure 3.4: On the left-hand side a 3D drawing of the spin rotator. The electric field is created by the left (blue) and right (turquoise) curved electrodes. The magnetic field is created by the top and bottom coils, which are represented here as red and orange blocks. In the background the electron beam exits into the electron optic, leading to the Mott analyser. The electron optics in front of the spin rotator is not shown. In the middle the top view of the left image. It shows the simulated electron beams paths with different starting positions and angles as blue traces. On the right-hand side an image of the build in spin rotator is shown. The electrons arrive through the cylinder in the back.

spin rotator so that the created magnetic field points along the y-component of the electron spin. Since the rotation of the electron spin in the fringing fields can not be calculated exactly we needed to experimentally determine it. For this purpose we used a perpendicularly magnetised sample and measured the spin polarisation while increasing the electric and magnetic fields of the spin rotator step by step. Due to the magnetic field the spin of the electron gets rotated, decreasing and increasing the detected out-of-plane and in-plane component, respectively. In this case the detected spin polarisation depends on the magnetic field inside the spin rotator in the following way

$$P(B) = P_0 \cos(\alpha) = P_0 \cos\left(\frac{leB}{m_e v}\right), \tag{3.12}$$

where P_0 is the beam polarisation when perfectly align with the detector axis. We know that the magnetic induction and therefore the rotation angle is directly proportional to the applied current I, which simplifies the formula to

$$P(I) = P_0 \cos(cI), \tag{3.13}$$

where $c = \frac{leB}{m_e v I}$. We measured the spin polarisation at the same position on the sample for different applied currents, as shown in Figure 3.5. By extracting the polarisation and plotting it versus the applied current we can fit the zero crossing, i.e., a 90° rotation, as shown in Figure 3.6. The fit yields for the zero crossing $I = 1.17\,\mathrm{A}$, which perfectly fits our calculations based on the simulations.

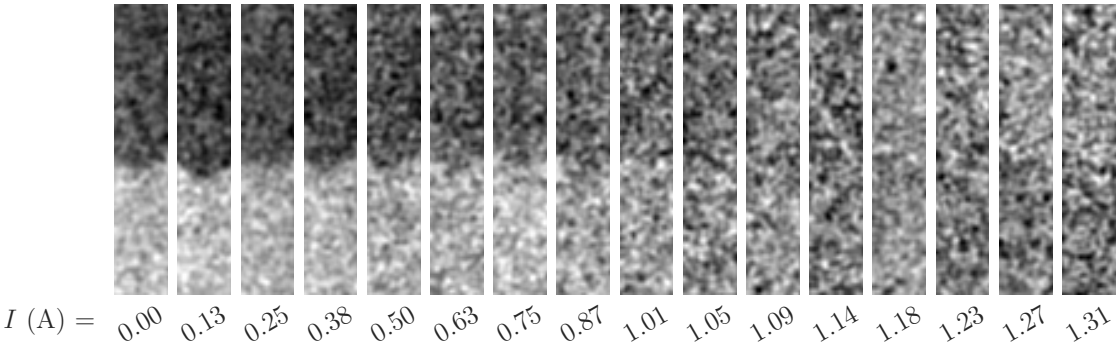

Figure 3.5: Spin-polarised micrographs of a perpendicularly magnetised sample at the same position for different applied currents. The out-of-plane component vanishes at around 1.14 A, after which the magnetic contrast reverses. The images were filtered with a Gaussian filter to enhance the contrast.

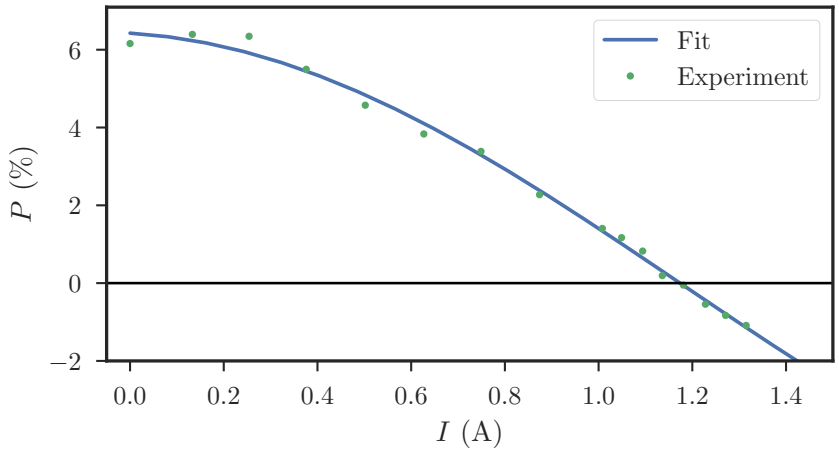

Figure 3.6: Spin-polarised micrographs of a perpendicularly magnetised sample at the same position for different applied currents at the spin rotator.

3.4 Sputter Removal

Scattering of the secondary electrons in paramagnetic material can lead to a loss of the spin polarisation. It is therefore crucial for spin-SEM to have as less as possible paramagnetic material on top of the specimen. For example when a sample is exposed to air a lot of unwanted particles (dirt) will deposit on the surface. In order to remove the dirt particles we use a sputter removal process. A so called “sputter gun” creates a flux of ions which are directed towards the sample to be cleaned. The ions collide with the surface atoms of the specimen and sputter them off. After the cleaning process we can check the material composition of the upper two nanometres with Auger electron spectroscopy in a target area.

As source for the ions we use an inert gas, however the ionising process can vary

depending on the requirements of the sputter process. When high sputter rates – the speed at which material is removed – are required a plasma is used as ion source. The plasma has a high density of ionised atoms, resulting in a high beam current ($\approx$1 mA). For lower sputter rates we use thermal electron emission to emit free electrons, which then ionise the inert gas in the space around it. The resulting beam current is much lower ($\approx$1 – 15 µA) than the one from "plasma guns".

The sputter rate depends not only on the number of electrons, but also on the energy of the electrons. The ion energy is set by an acceleration voltage, which varies from a view eV to several keV. The more energy the ions have the more destructive gets the sputter process, because the initial collision will erupt more energy and the ions penetrate deeper into the surface, thus colliding with more atoms. This results in rougher surfaces, which are preferable avoided for our purposes.

In our system we have tree different sputter removal guns: One plasma gun and two thermal electron emission guns. While the plasma gun and one of the electron emission guns ("top gun"), create a broad ion beam, which illuminates the whole sample, the last gun creates a focused ion beam ("focused gun"). The focused beam can be controlled with two deflection plates. By mapping the absorbed current, to the position of the beam an absorbed current micrograph can be constructed, allowing us to sputter only in a target area. The ion dose rates for the different guns are 8 mC m^{-2} s, 23 mC m^{-2} s and 2.3 C m^{-2} s for the focused gun, the top gun and the ion gun, respectively.

4 DMI in Perpendicularly Magnetised Thin Films

Even though nickel (Ni) or Fe on copper (Cu) are very well studied systems, their domain walls in the perpendicularly magnetised regime have never been investigated. This is mostly due to the fact that most magnetisation imaging techniques lack the resolution to resolve domain walls. In addition, theory predicts only Bloch domain walls in perpendicularly magnetised films independent of their thickness (without DMI in the system), rendering high resolution imaging of domain walls "uninteresting". In perpendicularly magnetised Fe/Ni/Cu(100) and Ni/Fe/Cu(100), however, chiral Néel domain walls have been found recently, which leads to the conclusion that Dzyaloshinskii–Moriya interaction must be present in these systems [44]. These findings are surprising since DMI is based on spin-orbit interaction and thus its strength scales with the spin-orbit parameter [23], which in turn is proportional to the atomic number to the power of four [15]. Fe, Ni and Cu have relatively low atomic numbers of 26, 28 and 29, respectively, which results in a small spin-orbit parameter compared to for example platinum (Pt), which is commonly used to create DMI in magnetic systems. However, when a sizeable DMI is present in Fe/Ni/Cu(100) and Ni/Fe/Cu(100) one can possible also expect one in similar systems, e.g. Ni/Cu(100). In perpendicularly magnetised systems the presence of DMI changes the preferred domain wall type from Bloch to intermediate or even Néel depending on its strength. When the DMI is created at the interface its energy contribution to the walls stays constant when increasing the magnetic layer thickness, other energy terms, however, change with the material thickness, which results in a vanishing contribution of the DMI to the domain walls for thicker magnetic materials. Our goal was to image domain walls in perpendicularly magnetised thin films and to directly identify a DMI contribution by analysing their wall type. We successfully did so by investigating Ni, Ni/Fe, Fe/Ni and Fe/Ni/Fe of different thicknesses on top of Cu(100) by spin-polarised scanning electron microscopy. For Ni/Fe/Cu(100) we found chiral Néel walls independent of the Ni thickness, therefore a strong DMI must be present. In the other systems we found chiral Néel domain walls for Ni thicknesses up to $\approx 3\,\mathrm{nm}$ and Néel, Bloch and intermediate walls above, revealing a weaker DMI compared to the Ni/Fe/Cu(100) system.

4.1 Sample Preparation

We use a Cu single crystal, which is recycled by removing old material by ion sputtering and then annealing at 870 K, which is necessary to get rid of the roughness created by the sputtering process. After thoroughly cleaning, the desired material can be deposited on

top. In our set-up we use thermal evaporation at room temperature for that purpose. At room temperature Fe grows on top of Cu in a face centred tetragonal (fct) ferromagnetic phase for up to 0.7 nm[†], which undergoes a transformation to face centred cubic (fcc) antiferromagnetic Fe for temperatures of 320 K and above. This antiferromagnetic order has a Curie-temperature of 250 K, thus being a paramagnet at room temperature. This antiferromagnetic fcc phase also exists between 0.7 nm and 2.0 nm at room temperature. For even thicker Fe a bcc ferromagnetic order forms with in-plane magnetisation [45].

Ni on Cu(100) grows in a fct ferromagnetic phase, the magnetisation is in-plane up to 1.2 – 1.8 nm [46–48], where a spin reorientation transition (SRT) takes place, turning the magnetisation into the out-of-plane direction. The thickness of Ni at which the SRT occurs can be controlled by temperature [49, 50], and, to a certain degree, by the atomic terraces of Cu, which in turn can be controlled by the annealing conditions [48].

The origin of the reorientation is the interplay between shape anisotropy K_s and magnetocrystalline anisotropy K. The former prefers an in-plane magnetisation while the latter can prefer in- or out-of-plane magnetisation depending on the Ni thickness. The magnetocrystalline anisotropy can be split up into a thickness-independent volume part K^V and a thickness-dependent surface contribution K^S/t, where t is the thickness. For thin Ni K^V favours an out-of-plane magnetisation and K^S an in-plane one [51]. In this thesis we stick to the convention that a positive constant favours out-of-plane magnetisation while a negative one favours in-plane magnetisation, i.e., $K^V > 0$, $K^S < 0$ and $K_s < 0$. For thicknesses below 1.2 nm, K^S/t together with the shape anisotropy K_s outweigh K^V, i.e., $K^V + K^S/t + K_s < 0$, thus the film is in-plane magnetised. Above this thickness, $|K^S/t|$ gets too small and the magnetisation turns in the out-of-plane direction. The origin of K^V favouring out-of-plane magnetisation is the lateral expansion of Ni on top of Cu(100) by 2.5 %, because a strain induced expansion of the lattice leads to a magnetic easy axis perpendicular to the strain axis [51]. The strain induced by the pseudomorphic growth starts to get released by misfit dislocations above a critical thickness [46, 52], which varies between 1.5 nm and 1.9 nm [47, 52], but even then still a partially pseudomorphic growth is present [53, 54]. The continuing strain relaxation is responsible for a lowering of the volume anisotropy K^V, which is visible in a decline in the perpendicular magnetocrystalline anisotropy, which starts at around 2.6 – 3.5 nm [47, 51]. When K^V gets too small to outweigh $K^S/t + K_s$ a second SRT can be observed, turning the magnetisation back into the plane. The thickness where the second SRT happens varies in literature between 6.0 nm [53] and 9.8 nm [47].

We evaporated Ni as a wedge by using a sliding shutter while evaporating. The Fe was usually evaporated as a thin layer, but sometimes also as a wedge. After evaporation we used Auger electron spectroscopy to analyse the surface. The spectra showed only small impurities of carbon (C) and sometimes negligible amounts of oxygen (O). From the peak heights of the evaporated material and the substrate one can calculate the thickness of the evaporated material. This was used to evaluate the rate of the evaporation and the wedge's slope. The rates were between 1 nm/h and 3.6 nm/h for Ni and 0.6 nm/h for

[†]For all thickness values in literature which were given in monolayer we used a monolayer spacing of 0.178 nm for Fe and 0.175 nm for Ni for the conversion to nanometre.

Fe. By controlling the speed of the sliding shutter we created Ni wedges with slopes varying between 1 and 4 nm/mm, resulting in a maximum Ni thickness of 7.2 nm. The thin underlaying Fe layer was between 0.1 nm and 0.2 nm thick, while the wedge had a maximum thickness of 0.3 nm. For the top Fe layer Auger spectra analysis showed a thickness of ≈0.2 nm but also contamination with ≈0.4 nm C, which results in an inaccurate determination of the thickness. The measurements for the underlying Fe layer yielded (0.11 ± 0.01) nm. However, nominally the top and bottom Fe layer were evaporated under similar conditions, only a ∼13 K higher crucible temperature during the second evaporation was noticed which can not explain such a big discrepancy, thus we assume that the layers are equally thick and the difference in the measurements is related to contamination.

4.2 Domain Walls in Ni/Cu(100)

We imaged domain walls in 1.6- to 6.5-nm-thick Ni, which exhibits a perpendicular magnetisation. Interestingly we found domain walls showing the magnetisation configuration of Bloch, Néel and intermediate walls. For thin Ni up to 4 nm imaged domain walls had very weak magnetic in-plane contrast, even though in the out-of-plane component no significant difference to thick Ni was found. Within the experimental uncertainties the images in this thickness range revealed only Néel domain walls, one example is shown in Figure 4.1.

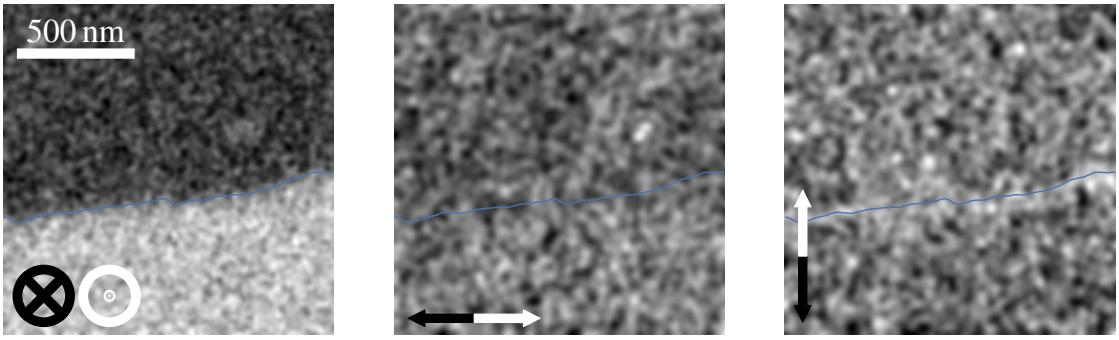

Figure 4.1: Spin-polarised micrographs of a Néel type domain wall in 2.2-nm-thick Ni/Cu(100). The Néel component of the domain wall has a right-handed chirality. The graphs were filtered with a Gaussian filter for better visibility and the position of the domain wall extracted from the out-of-plane component was indicated by the blue line.

Domain fluctuations as observed recently [55] could cause a reduction of the in-plane contrast, while the out-of-plane component distant from the domain wall would remain the same. The in-plane component in Figure 4.1 is about 10 to 15 % of the out-of-plane value. If we describe fluctuations around the domain wall with a normal distribution, a standard deviation ten times bigger than the domain wall width will be necessary to reduce the in-plane contrast to about that level. However, the domain wall will appear

significantly wider (more than a factor 10), which will be easily detectable in the out-of-plane component. Additionally domain wall fluctuations seem to appear mainly at specific positions of the domain wall not along its whole length [55]. A similar argument holds for domain fluctuations between two distinct pinning sites. If the pinning sites are laterally distinguishable with the spin-SEM we will measure two domain walls with their in-plane polarisations summing up to 100 % of the out-of-plane value and again a wide domain wall in the out-of-plane component. When the pinning sites are not distinguishable the signals will overlap and the value of the polarisation will get closer to the out-of-plane value. Therefore we can exclude domain wall fluctuations as the origin of the reduced magnetic contrast. We have not figured out another possible cause yet, thus the low in-plane contrast remains an open question.

For thicker Ni we found in addition intermediate and Bloch like domain walls. Due to weak magnetic contrast an exact determination of the magnetic moment angle ψ of the wall was not possible, however, within the experimental uncertainty we can distinguish between Néel, Bloch or intermediate domain walls. Nevertheless, the discovery of anything else than a Bloch wall can only be explained by assuming that DMI is present in the system or by the presence of a vicinal surface, which changes the symmetry of the anisotropy from a four-fold to a two-fold one.

We were able to exclude the latter case by rotating the Cu crystal by 90° before evaporation and repeating the experiment. The orientation of the magnetisation in the domain wall showed no dependence on the crystallographic axis of the crystal. Additionally, we also measured domain walls of the same type perpendicularly orientated to each other. Thus DMI must be responsible for the creation of Néel and intermediate domain walls in Ni/Cu(100). By analysing the spin-polarised micrographs shown in Figure 4.2 one can identify a domain wall with in-plane components in both directions - an intermediate domain wall. The Néel component of this wall as well as all other walls

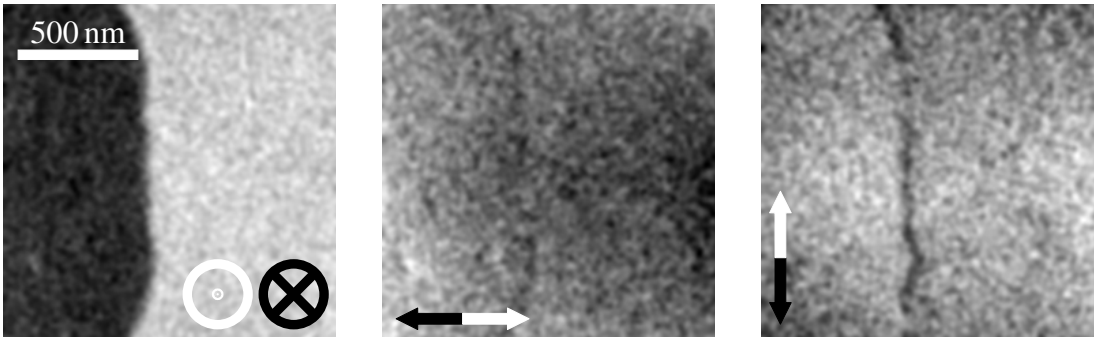

Figure 4.2: Spin-polarised micrographs of an intermediate domain wall with a strong Bloch component in 6.2-nm-thick Ni/Cu(100). The Néel component of the domain wall has a right-handed chirality. The images were filtered with a Gaussian filter for better visibility.

measured show right-handed chirality, which is another strong indication for DMI in the

system as discussed in section 2.3.

4.3 Domain Walls in Ni/Fe/Cu(100)

Interfacial DMI strongly depends on the interface where layers meet. By inserting different materials at the interface one can manipulate the DMI constant and therefore force a different behaviour of the domain walls. We added Fe at the interface between Ni and Cu. This was done recently for thin films with Ni between 0.18 and 1.75 nm and Fe between 0.23 and 0.45 nm, where a right-handed chirality for Fe/Ni/Cu and a left-handed chirality for Ni/Fe/Cu was discovered [44].

We imaged domain walls at Ni thicknesses between 1.6 and 6 nm. All investigated domain walls were Néel type with a right-handed chirality, e.g. Figure 4.3. Since DMI

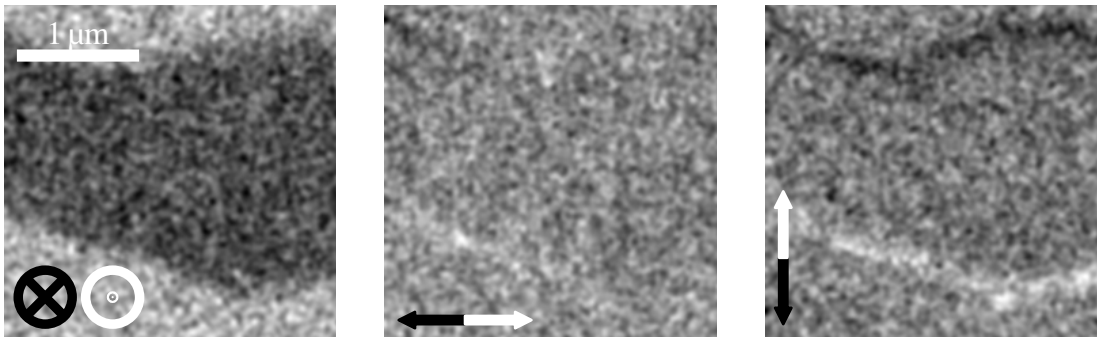

Figure 4.3: Spin-polarised micrographs of two Néel domain walls close to the SRT in Ni(1.6 nm)/Fe(0.1 nm)/Cu(100). The domain walls have a right-handed chirality. The images were filtered with a Gaussian filter for better visibility.

energetically prefers Néel domain walls, the DMI constant here must be larger than for Ni/Cu(100). Surprisingly, the constant has a different sign, i.e., the walls have a different chirality, than in earlier measurements [44].

4.4 Domain Walls in Fe/Ni/Cu(100) and Fe/Ni/Fe/Cu(100)

In order to learn more about which interface plays the dominant role we investigated the systems of section 4.2 and section 4.3 with additional 0.11 nm Fe as a top layer.

Fe/Ni/Fe/Cu(100)

In Fe/Ni/Fe/Cu(100) we imaged domain walls between 2.8-nm- and 5.1-nm-thick Ni. For 2.8-nm-thick Ni we found a Néel domain wall, while for thicker Ni we found intermediate and Bloch type domain walls. Néel and intermediate domain walls showed a right-handed chirality, which is the same as in Ni/Cu and Ni/Fe/Cu. In Figure 4.4 a domain wall at 3.3-nm-thick Ni is shown. Both in-plane components show a clear signal at the

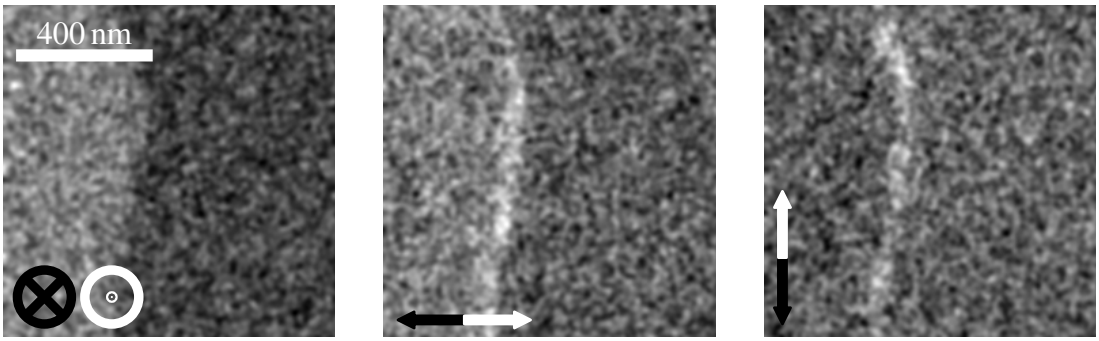

Figure 4.4: Spin-polarised micrographs of an intermediate domain wall at a Ni thickness of (3.3 ± 0.2) nm in Fe/Ni/Fe/Cu(100). The domain wall has a right-handed chirality. In the x-component the out-of-plane component is slightly visible, which we attribute to a small misalignment of the sample. The graphs were filtered with a Gaussian filter for better visibility.

position of the domain wall, i.e., the domain wall type is intermediate with a right-handed chirality. The Ni is now sandwiched by the same material, namely Fe, therefore to first approximation no interfacial DMI is expected because the system is now symmetric. Even if the top Fe would be a bit thicker a reverse chirality is expected compared to Ni/Fe/Cu(100).

Fe/Ni/Cu(100)

In Fe/Ni/Cu(100) a reversed chirality to Ni/Fe/Cu(100) is expected, if the DMI is a result of the Ni/Fe interface, as suggested in recent experiments [44]. However, as shown in Figure 4.5 we find walls with the same chirality as in all our other experiments, i.e.,

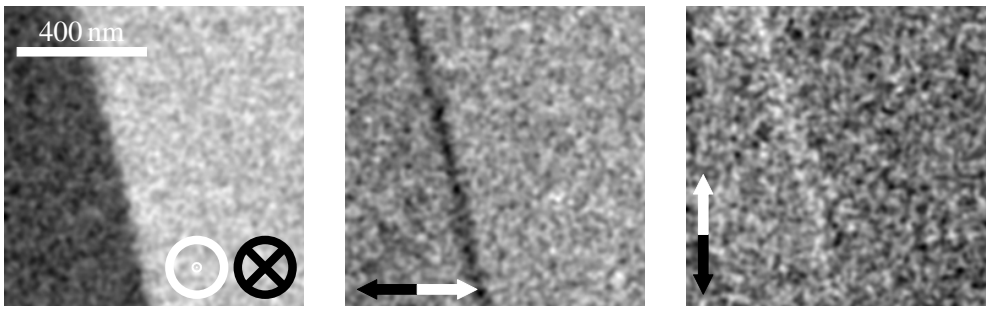

Figure 4.5: Spin-polarised micrographs of a intermediate domain wall in Fe/Ni/Cu(100). The Ni at this position was (4.8 ± 0.3) nm thick. The wall shows a right-handed chirality. The graphs were filtered with a Gaussian filter for better visibility.

a right-handed chirality. Additionally, we fit the domain wall profile with Equation 2.6.

Therefore we rotate the scans until the domain wall is parallel to the y-axis, then we take the average magnetisation along the y-direction, which results in an averaged linescan across the domain wall. The data as well as the fits are shown in Figure 4.6. In order to

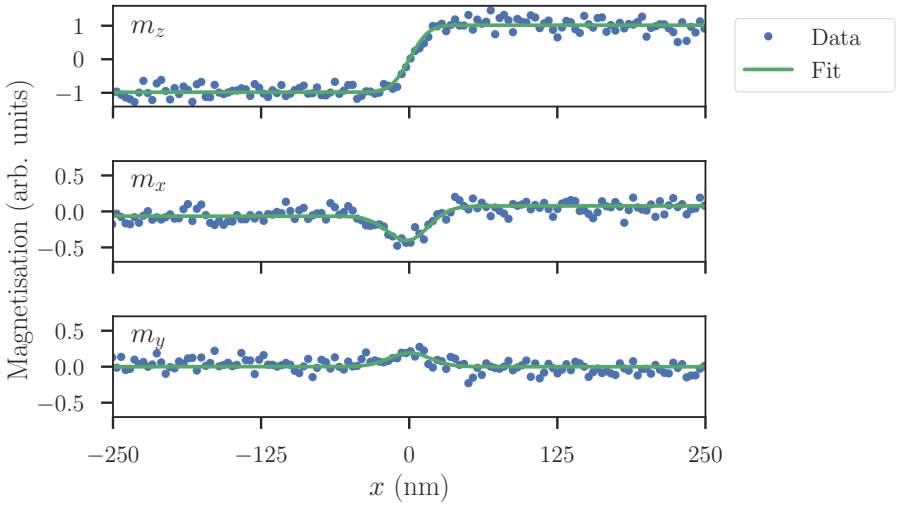

Figure 4.6: Averaged linescans across the domain wall of Figure 4.5 and their corresponding fit. The fit yields a domain wall width $\Delta = (6.2 \pm 0.8)\,\mathrm{nm}$ and an azimuthal angle $\psi = (142 \pm 6)°$.

take the finite resolution of the microscope into account we assumed a Gaussian beam profile while fitting, i.e., we used as fitting function a convolution of the components m_i and a normal distribution ($f(x) = (2\pi\sigma^2)^{-1/2}\exp(-x^2/2\sigma^2)$) with a standard deviation σ. We find for the domain wall width $\Delta = (6.2 \pm 0.8)\,\mathrm{nm}$ and for the azimuthal angle $\psi = (142 \pm 6)°$.

The addition of Fe at the top surface has no significant effect on the domain wall structure compared to Ni/Cu(100). When the DMI created at the Fe/Ni interface would be of the same strength as at the Ni/Cu(100) interface but of different sign, the formation of Bloch domain walls is expected, since the effect of both interfaces cancels out. If the DMI would have the same sign, similar behaviour as in Ni/Fe/Cu(100) is expected. Thus, most likely the Fe/Ni interface creates no or very little DMI.

4.5 Domain size

As briefly discussed in section 2.3 the size of the domains depends on the magnetic material thickness: The closer the material thickness is to the SRT the smaller the domains get. This behaviour shows an exponential dependence on the material thickness. A typical domain formation near the SRT is shown in Figure 4.7. We used this image to determine the average domain size in dependence of the material thickness. Therefore we divided the actual length of the red lines by the number of domains along them to get the average domain width. Since we know that the domain width depends on the energy

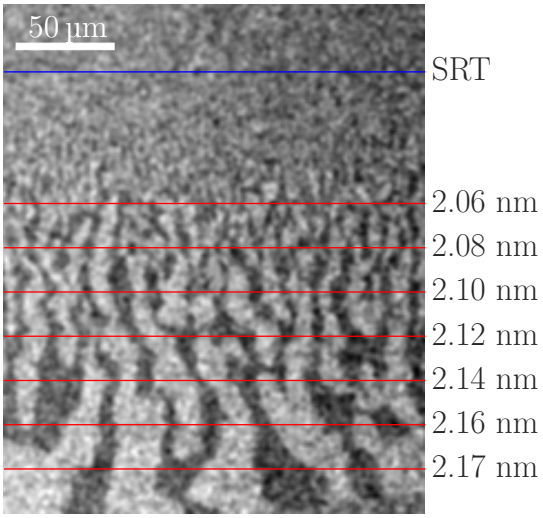

Figure 4.7: Out-of-plane domain pattern close to the SRT, which is at a total magnetic material thickness of 2.00 nm. The material stack here is Ni/Fe/Cu(100), the underlying Fe layer is (0.14 ± 0.06) nm thick. Dividing the length of the red lines by the number of domains for each of them yields the average domain size. The total magnetic material thickness is shown next to the lines.

of the domain wall we can calculate the DMI. When we insert the domain wall energy $\sigma = 4\sqrt{AK_{eff}} - \pi D$ in Equation 2.12 and use the parameter for the stripe domain phase we get

$$W = 0.955t \exp\left(\frac{4\sqrt{AK_{eff}} - \pi D}{\mu_0 M_s^2}\right). \tag{4.1}$$

We can calculate the effective anisotropy with $K_{eff} = K^V + K^S/t - \mu_0 M_s^2/2$ [27], where $K^V = (30 \pm 3)\,\mu\text{eV/atom}$ [47] is the bulk anisotropy constant, and K^S the surface anisotropy constant which will be used as fitting parameter. In order to estimate the exchange stiffness we take the bulk values of Ni $A_{\text{Ni}} = 8.2\,\text{pJ m}^{-1}$ [56] and $A_{\text{Fe}} = 25\,\text{pJ m}^{-1}$ [57] and weight them by their relative thickness, i.e., $A = (A_{\text{Ni}}t_{\text{Ni}} + A_{\text{Fe}}t_{\text{Fe}})/t$, where t_{Ni}, t_{Fe} and t are the thicknesses of Ni, Fe and their sum, respectively.

Similarly we estimate the saturation magnetisation M_s. In order to do so we use the magnetic moments determined in literature to calculate M_s. Even though in literature for thin films usually a value of the saturation magnetisation equal to the bulk value is assumed, early Hall resistance measurements [58] of Ni as well as recent x-ray magnetic circular dichroism measurements of Ni [59] and Fe [60] on Cu(100) suggest that the saturation magnetisation changes for thin films. Srivastava *et al.* [59] found for 0.75-nm-thick Ni a magnetic moment of $\mu_{\text{Ni}} = (0.3 \pm 0.1)\mu_B$, where μ_B is the Bohr magneton, which is less than 50 % of the bulk value $\mu_{\text{Ni,bulk}} = 0.64\mu_B$. For Fe on the other hand a magnetic moment $\mu_{\text{Fe}} = (3.71 \pm 0.1)\mu_B$ was found for 0.68-nm-thick Fe by Dunn *et al.* [60] which is a significant increase compared to the theoretical value $\mu_{\text{Fe,theory}} = 2.78\mu_B$

for fcc Fe. The Fe layer in our case is only 0.1 nm, thus we choose $\mu_{\mathrm{Fe}} = (3.71 \pm 0.1)\mu_B$ for our calculations.

Which value we should chose for Ni is ambiguous, most likely $(0.3 \pm 0.1)\mu_B$ is too low for our 4.8-nm-thick Ni as the growth is not pseudomorphic anymore. The bulk value is probably too large, because strain is still present in the system and therefore the bulk crystal order is not yet reached. We use these two values to estimate a minimal ($M_{s,min}$) and maximal ($M_{s,max}$) saturation magnetisation as follows:

$$M_s = n\frac{\mu}{a^3} = n\frac{\mu_{\mathrm{Ni}} t_{\mathrm{Ni}} + \mu_{\mathrm{Fe}} t_{\mathrm{Fe}}}{t a^3}, \tag{4.2}$$

where μ is the magnetic moment, a the lattice constant and n the number of atoms per unit cell. In order to account for the different thicknesses of Fe and Ni we weight their magnetic moments by the relative magnetic material thickness. We assume that the DMI originates at the interface, where the growth is still fully pseudomorphic, therefore we use the lattice constant of fcc Cu $a = 361.49\,\mathrm{pm}$ of a unit cell containing four atoms. Thus we calculate for the saturation magnetisation $M_{s,min} = 4 \cdot \mu/(361.49\,\mathrm{pm})^3 = 290\,\mathrm{kA\,m^{-1}}$ and $M_{s,max} = 552\,\mathrm{kA\,m^{-1}}$. Finally we can fit the data points as shown in Figure 4.8. As

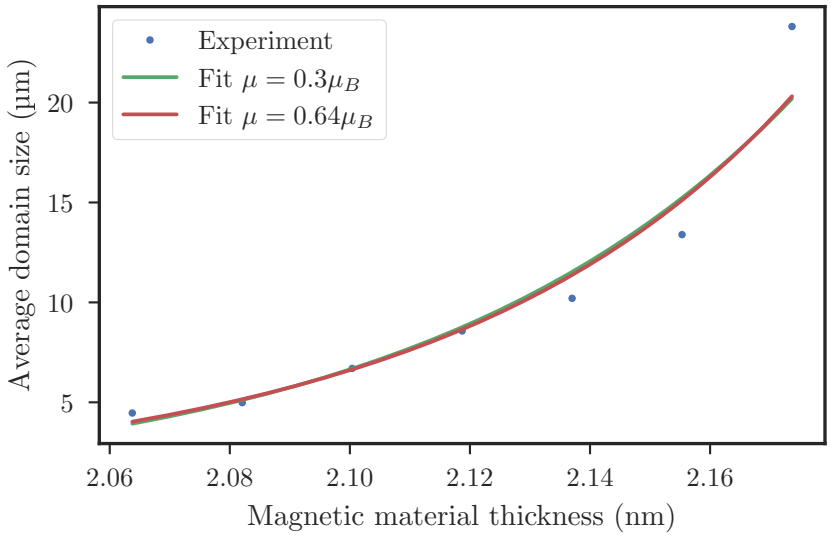

Figure 4.8: Average domain size vs. the combined magnetic material thickness of Fe and Ni. The experimental data is displayed as points, whereas the fits are the continuous lines.

fitting parameters only K^S and D are left, whose values acquired by the fit are summarised in Table 4.1. The results show that the model does not work for our measurement as the errors are much larger than the values themselves. Note that the fit gave better results when a positive K^S was allowed, however, in perpendicularly magnetised Ni K^S has to be negative. The model probably failed because the domain size was too big, or in other words the data points too far from the SRT and the model is only valid in close vicinity to the SRT. The resolution of the image was not sufficient enough to determine

Table 4.1: Fitting results for domain width vs. magnetic material thickness

	D ($\mathrm{mJm^{-1}}$)	K^S ($\mathrm{mJm^{-2}}$)
$\mu_{\mathrm{Ni}} = 0.3$	1 ± 5	-0.3 ± 1.3
$\mu_{\mathrm{Ni}} = 0.64$	0.7 ± 2.8	-0.02 ± 0.77

the domain size closer to the SRT. Therefore we need dedicated measurements with higher resolution close to the SRT. Fitting the data with another approach [61] also did not yield reasonable results.

4.6 Discussion and Conclusions

Investigation of perpendicularly magnetised thin films and stacks of Fe and Ni on top of the Cu(100) surface revealed chiral intermediate and Néel domain walls in addition to the Bloch walls predicted by theory. We ruled out a crystallographically preferred direction of the Cu crystal, which would influence the domain wall type. The different wall types, therefore, can only be explained by the presence of DMI in the system. Even though DMI was found already in thin Ni/Fe/Cu(100) and Fe/Ni/Cu(100) [44] this is somewhat surprising since DMI was mostly observed in systems with layers of heavy atoms, e.g. Pt, because the spin-orbit parameter scales with the atomic number to the power of four. The relative light elements Fe, Ni and Cu cause in theory only a weak DMI. Chen *et al.* [44] found a DMI arising at the interfaces of Ni/Fe/Cu(100) and Fe/Ni/Cu(100) causing pure Néel walls with a left-handed and right-handed chirality, respectively. In our case we find intermediate and Néel domain walls in up to 7-nm-thick Ni. However, a weak interfacial DMI presumably would have negligible influence at such ticknesses. Additionally, the sign of D we found is opposite to [44]. An experiment with a thick underlying Fe layer similar to the thickness of Chen *et al.* still resulted in a opposite chirality. The Ni thickness was larger than the one from Chen *et al.*, but it is unlikely that with increasing Ni thickness the sign of D changes. Furthermore, first experiments in which we replaced Fe by cobalt (Co) also showed a right-handed chirality.

Even though the sign of the DMI is opposite we can compare its absolute value. In our set-up only a few methods for the determination are applicable. Unfortunately, a method by domain expansion [62, 63] was hindered by the strong pinning potential at the surface. An estimate via the domain size yielded imprecise results, probably related to the date points being too far from the SRT. Additionally, an estimate for intermediate walls with the critical value of the DMI $D_c = 2t \ln(2) \mu_0 M_s^2 / \pi^2$ as defined in Equation 2.11 can be made. As an example we use the domain wall in 4.8-nm-thick Ni from Figure 4.5 and its fitted parameters (Figure 4.6), namely the domain wall width $\Delta = (6.2 \pm 0.8)\,\mathrm{nm}$ and the azimuthal angle $\psi = (142 \pm 6)^\circ$, which is equivalent to $(38 \pm 6)^\circ$ for our considerations.

We use the values of the saturation magnetisation $M_{s,min} = 290\,\mathrm{kA\,m^{-1}}$ and $M_{s,max} =$

$552\,\mathrm{kA\,m^{-1}}$ (as calculated above) in Equation 2.11 to calculate

$$D_{c,min} = (0.071 \pm 0.005)\,\mathrm{mJ\,m^{-2}} \text{ and}$$
$$D_{c,max} = (0.26 \pm 0.02)\,\mathrm{mJ\,m^{-2}}.$$

Note that the errors are related to the uncertainty in the material thickness, but since the largest error is caused by the choice of the magnetic moment we will omit the errors in the following. The difference for this two extreme cases is large, which shows us already that it is crucial to know all the material parameters as precisely as possible to give a good estimate of D. For further considerations we use the mean value of $D_c = (D_{c,min} + D_{c,max})/2 = 0.17\,\mathrm{mJ\,m^{-2}}$. For intermediate domain walls D can be calculated via the magnetic moment angle ψ, i.e., $D = D_c \cos(\psi)$ [9], which results in $D = 0.13\,\mathrm{mJ\,m^{-2}}$ for Fe(0.1 nm)/Ni(4.8 nm)/Cu(100). Interestingly, when we compare that to the exchange stiffness $A = 9.3\,\mathrm{pJ\,m^{-1}}$ of our system we find that $Da/2 = 0.23\,\mathrm{fJ\,m^{-1}}$ is about 400 times smaller. Nevertheless it has a significant influence on the energy landscape and can disturb the parallel alignment preferred by the Heisenberg exchange interaction.

Chen *et al.* [44] found a value $D = 0.12$-$0.17\,\mathrm{meV}$ per atom. Even thought their Fe and Ni layers are both thinner than 2 nm they use bulk values of the magnetic moments for the estimate of D, i.e., $\mu_{\mathrm{Fe}} = 2.6\mu_B$ and $\mu_{\mathrm{Ni}} = 0.6\mu_B$. To compare our DMI value with theirs we recalculate D with these values, i.e., $D = (0.17 \pm 0.02)\,\mathrm{mJ\,m^{-2}}$, and per atom $D = (0.17 \pm 0.02)\,\mathrm{mJ\,m^{-2}} \cdot (361.49\,\mathrm{pm})^2/2e = (0.069 \pm 0.005)\,\mathrm{meV}$, where the "2" in the equation arises from two atoms per unit cell. Even though our value is "only" 50 % off the value of Chen *et al.*, and therefore suggests that we are in good agreement, Chen *et al.* underestimate their value while we most likely overestimate it due to the bulk magnetic moments.

The discrepancy in the absolute values of D might result from the different interfaces. We use less than one monolayer of Fe at the top and in between Ni and Cu. In the case of Ni/Fe/Cu this should probably be considered as Ni/$\mathrm{Ni}_{1-x}\mathrm{Fe}_x$/Cu, which could probably explain the enhancement of the DMI we found in our experiments. In the case of Fe/Ni/Cu the few Fe atoms on the top apparently have a negligible effect. In the case of Fe/Ni/Fe/Cu there are two different interfaces, which is probably why they do not compensate each other.

All these considerations are based on the assumption that the DMI is created at the interface. However, the symmetry can also be broken in the volume. Since we see misfit dislocations for thick Ni and no misfit dislocations for thin Ni there must be a structural symmetry breaking. Depending on in which direction the symmetry is broken DMI arises in a specific direction. We can use the rules of Moriya to determine in which direction the DMI is pointing [3]. If the symmetry is broken along the wedge direction, then the DMI vector will lie in the plane perpendicular to this direction. If the symmetry is broken along the sample normal, the DMI vector will lie in the plane. This is the same direction as a DMI created at the interfaces of the different materials. Such a symmetry breaking could be created by a strain varying from atomic layer to atomic layer. Recent calculations for three layers of bcc Fe with a difference in strain from layer to layer of

0.1 % resulted in a DMI value of 0.035 meV per atom [22]. If we compare this to our estimate of $D_{c,min} = 0.03$ meV we see that this theory could explain why we still observe intermediate domain walls for thick Ni. Calculations for fct Fe and Ni on Cu(100) could shed light on our results.

5 Bloch to Néel Wall Transition in Perpendicularly Magnetised Nanowires

In perpendicularly magnetised films without Dzyaloshinskii–Moriya interaction the preferred domain wall type is Bloch independent of the film thickness as discussed in chapter 4. In in-plane magnetised materials the domain wall type depends on the thickness of the material [5, 6]. In the 1D model the transition happens abrupt, but already Aharoni [6] realised that this is due to limitations by the one-dimensionality of the model, since in a certain thickness range cross-tie domain walls form [5]. Also other domain formations like continuous asymmetric deformations [64] and zigzag patterns [1] can be observed.

In out-of-plane magnetised materials the domain wall type can be changed from Bloch to Néel by laterally confining the wall. This was done in flat nanowires (nanostripes) by adding constrictions [65] or by shrinking the dimensions [66–68], i.e., decreasing the thickness or width of the nanostripes. Measuring the anisotropic magnetoresistance (AMR) of nanostripes with and without domain wall was the only experimental work about the Bloch to Néel wall transition. The authors repeatedly compared the resistance of two wires, one with a domain wall and one without a wall. They found for wire widths of 59 nm and below a difference in the resistances and attributed this to the appearance of Néel walls [66]. A direct observation of this transition in real space is missing. Both Bloch and Néel walls were observed in thin films by spin-polarised scanning tunnelling microscopy [69], in a multilayer by spin-polarised low-energy electron microscopy [44], and in nanowires by optically monitoring the Zeeman shift of the electron spin in a nitrogen-vacancy defect in diamond [70].

In collaboration with the Condensed Matter Physics Group of Bryan Hickey from the School of Physics and Astronomy of the University of Leeds we investigated perpendicularly magnetised Co/Ni multilayer systems. The results of the investigations were summarised in a manuscript and published recently [71]. Our goal was to directly image the Bloch to Néel wall transition in nanostripes by spin-polarised scanning electron microscopy. Therefore we confined the Co/Ni multilayer system to wires of different width by structuring with electron-beam lithography. We found a Néel wall in a 57-nm-wide wire, Bloch walls in wires above 92 nm width and an intermediate domain wall in a 70-nm-wide wire. The appearance of an intermediate wall can only be explained by a transition which happens by continuously rotating the magnetic moment angle ψ from Bloch to Néel configuration, unpredicted by established theoretical models. We corroborate this finding by comparing it to micromagnetic simulations and analysing the individual energy contributions, which also helps to exclude the existence of Dzyaloshinskii–Moriya interaction in our system.

5.1 Structural and Magnetic Characterisation

A Co/Ni multilayer as magnetic material was chosen because the magnetic properties can be tuned by changing the thicknesses of the individual layers, the number of repetitions i and the adjacent non-magnetic layers. As basis we used the stack Pt/Co/[Ni/Co]$_i$/Pt(3 nm)/Ta(5 nm)/SiO$_x$(6 nm)/Si, which we modified by varying the number of repetitions i, the thicknesses of the individual layers in the multilayer stack and the thickness of the upper Co and Pt layer. After the growth we characterised the magnetic properties of the samples with superconducting quantum interference device (SQUID) and magneto-optical Kerr effect (MOKE) measurements and the layer thicknesses with low-angle x-ray diffraction. SQUID and MOKE were used to verify the magnetic easy-axis and to estimate the perpendicular anisotropy K_u and the saturation magnetisation M_s. We used the results as first estimate because the samples which were intended for structuring were laterally to big for a precise SQUID measurement.

Prior to magnetic imaging, the samples were sputtered with a xenon ion beam of 1 keV energy at normal incidence and a beam dose of $\approx 1.7\,\mathrm{C\,m^{-2}}$ in order to remove one nanometre of the Pt capping layer. We controlled the sputtering process by monitoring the material composition of the surface by Auger electron spectroscopy. Nevertheless, the sputtering also results in an inevitable atomic scale mixing, which reduces the perpendicular anisotropy. We sputter cleaned a sample and removed it from the UHV system after capping it with gold to measure M_s and determine K_u after sputtering. The results for Pt(1.5 nm)/Co(0.55 nm)/[Ni(0.7 nm)/Co(0.4 nm)]$_3$ were a saturation magnetisation of $(5.7 \pm 0.2) \times 10^5\,\mathrm{A\,m^{-1}}$ and a perpendicular anisotropy of $(2.5 \pm 0.4) \times 10^5\,\mathrm{J\,m^{-3}}$.

5.2 Structuring

The nanowires were created from a film by physical etching through a mask, which was fabricated by electron-beam lithography (EBL) and lift-off. A sketch of the process is shown in Figure 5.1. As basis a silicon (Si) substrate covered with the stack including the Co/Ni multilayer was used (Figure 5.1 (a)). As first step the sample was thoroughly cleaned with acetone followed by isopropyl alcohol (IPA). A positive electron-beam (e-beam) resist (polymethyl 2-methylpropenoate (PMMA) AR-P 672.02) was homogeneously coated on top of the sample in a spin coater (40 s at 4000 rpm), resulting in a 70-nm-thick layer of resist (Figure 5.1 (b)). Subsequently the sample was baked at 180 °C for 30 min to remove the anisole, which acts as carrier liquid for the PMMA. Targeted areas were exposed to a dose of $\approx$400 mC cm^{-2} by scanning with a 100 keV electron beam. The resist in the exposed areas was removed by first developing the sample in a 1:2 mixture of Methyl isobutyl ketone and IPA, second cleaning the sample in IPA and third by 400 W oxygen plasma ashing for 20 s (Figure 5.1 (c)). The material for the mask, i.e. 15 nm of Al, was deposited by thermal evaporation, covering the whole sample and thereby filling the holes (Figure 5.1 (d)). N-Methyl-2-pyrrolidone was used in a 30 min lift-off process at 110 °C to remove the remaining resist and thereby th Al on top of the resist (Figure 5.1 (e)). The top few nanometres of the material were

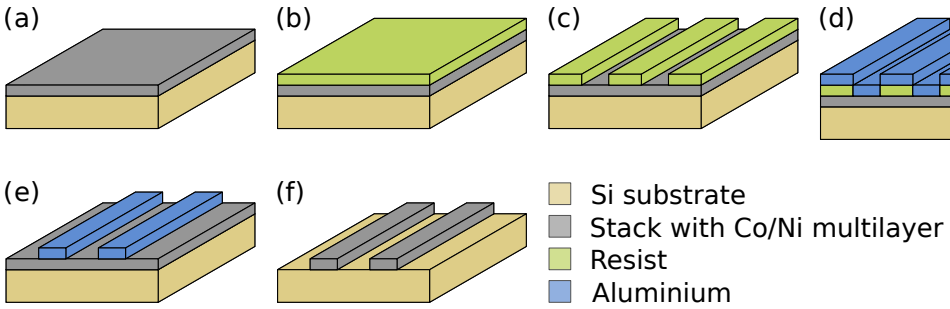

Figure 5.1: Sketch of the different steps of the EBL process. (a) Si substrate covered with the material to be patterned, i.e., the stack with the Co/Ni multilayer. (b) A thin layer of e-beam resist was spun on top with a spin coater. (c) Areas of the resist were exposed to an electron beam and developed. (d) Al was deposited. (e) After a lift-off process only the Al remains on top of the material stack. (f) The structures after etching and cleaning.

then striped by unidirectional ion milling. In order not to damage the magnetic material the milling parameters were chosen such that after the process a bit Al remained, which was then removed by dipping the samples for 20 s into AZ 400K optical resist developer (Clariant) (Figure 5.1 (f)).

We created different shaped structures, e.g., squares, triangles, and most importantly different sized bow-tie shaped nanowires (see Figure 5.2). These were intended for trapping the domain wall close to the centre of the constriction upon application of an alternating perpendicular field to inject domain walls from adjacent large pads.

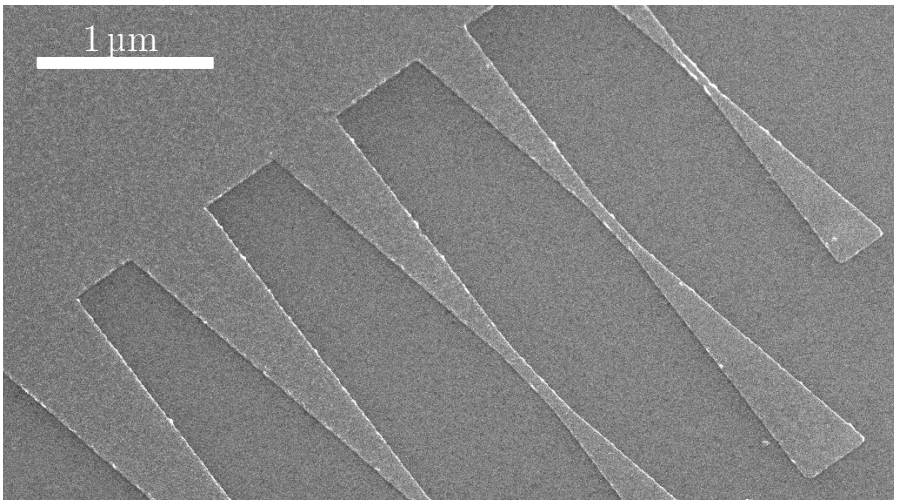

Figure 5.2: SEM image of bow-tie shaped magnetic nanowires attached to a large pad.

5.3 Bloch Walls in Extended Square Structures

When investigating the domain wall type in dependence of lateral dimensions one has also to consider the case of an infinite plane (film). The domain wall type found here is a first indication if Dzyaloshinskii–Moriya interaction prevails in the system. For that purpose we measured domain walls in a 400 µm × 400 µm pad, which otherwise is used to measure Auger spectra. The magnetisation components are shown in Figure 5.3.

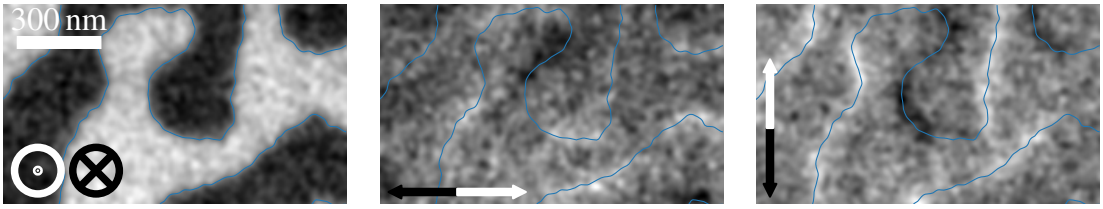

Figure 5.3: The magnetisation configuration in a 400 µm × 400 µm Co/Ni pad. The position of the domain walls from the out-of-plane component extracted is indicated by the blue lines. The magnetisation in the domain walls is always pointing along the wall, i.e., only Bloch walls form.

The magnetic moment in the walls always points along the wall, i.e., we only found Bloch domain walls. Additionally, we investigated the domain walls in smaller pads of 2.7 µm × 2.7 µm size (Figure 5.4). Even though the x-component is missing, the domain

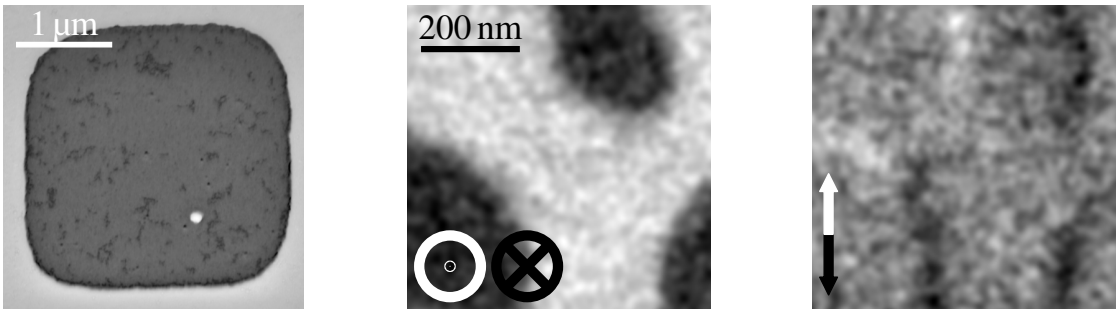

Figure 5.4: On the left-hand side a SEM micrograph of pad made out of Co/Ni multilayer with an area of 2.7 µm × 2.7 µm. The magnetisation configuration is shown for the centre of the pad.

walls shown must be Bloch walls, because no magnetic signal is present at the positions where the wall is aligned horizontally.

5.4 Domain Walls in Dependence of Wire Width

In order to investigate the Bloch–Néel wall transition we imaged domain walls in nanostripes with widths between 57 nm and 300 nm, in the following we will concentrate on

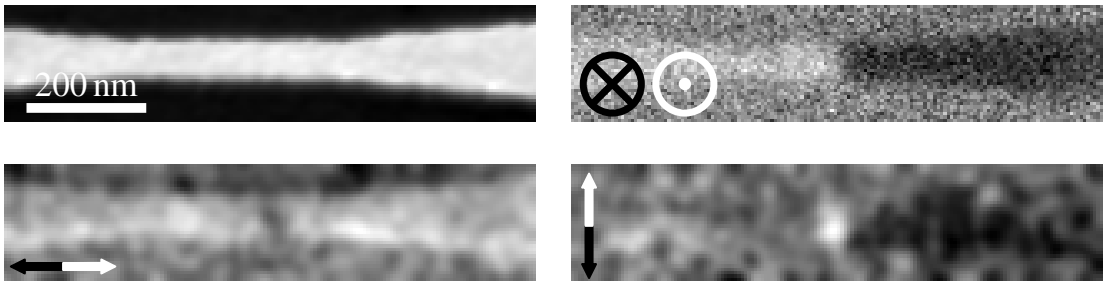

Figure 5.5: Scanning electron micrographs of a 70-nm-wide ferromagnetic "bow-tie" nanowire. A domain wall is found at the narrowest part of the wire, where also the wire width of 70 nm is measured. The wall has magnetisation components in both in-plane directions. In addition, a slight canting of the domain wall is observed. The images of the in-plane component were Gaussian filtered to highlight the domain wall.

the results from a of 70-nm-wide wire, which is shown in Figure 5.5. The wire width was determined at the position of the domain wall directly from the scanning electron micrograph with an uncertainty of 5 nm. The domain wall shown in Figure 5.5 has magnetisation components in both in-plane directions, thus it is an intermediate domain wall. A closer look also reveals that the domain wall is inclined by $(11 \pm 6)^\circ$ with respect to the wire's cross section. We fitted the magnetisation components m_i with the domain wall profile from Equation 2.6 as shown in Figure 5.6. Similar to section 4.4 we assumed a Gaussian beam profile while simultaneously fitting the profiles and we find $\sigma = 13\,\mathrm{nm}$, $\lambda = (11 \pm 2)\,\mathrm{nm}$ and $\psi = (135 \pm 5)^\circ$ for the 70-nm-wide wire. For classifying the wall type we restrict ourselves to angles between 0 and 90°, e.g., $\psi = (135 \pm 5)^\circ$ is equivalent to $\psi = (45 \pm 5)^\circ$. Therefore, in the following we will display ψ always as the smallest multiple. A small asymmetry in the measurement of the m_y component is present, corresponding to a rotation of $(5 \pm 1)^\circ$ of the secondary electrons, which we attribute to a combination of a misalignment of the sample normal with respect to the detector axes and spin rotation through the electron optics.

Similarly, we fitted the profile of the domain walls in a 57-nm, a 93-nm and a 300-nm wide nanowire as shown in Table 5.1. We observe Bloch walls in nanowires of 93-nm

Table 5.1: Results of fitted domain wall profiles

Nanowire width (nm)	λ (nm)	ψ (°)
57	9 ± 2	5 ± 12
70	11 ± 2	45 ± 5
93	7 ± 2	90 ± 10
300	9 ± 2	89 ± 14

width and above, a Néel wall in the 57-nm and an intermediate wall in the 70-nm-wide

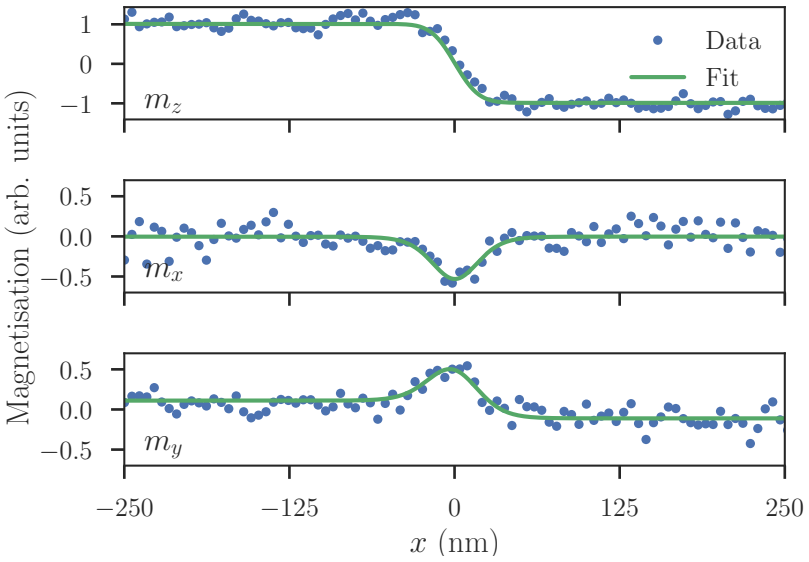

Figure 5.6: The magnetisation profiles $m_i(x)$ $(i = x, y, z)$ of the 70-nm-wide nanowire as a function of the distance from the centre of the wall. The perpendicular and in-plane magnetisation components were fitted with the 1D domain wall model and considering the finite resolution of the microscope.

wire.

In the 1D domain wall model, the demagnetising energy determines whether a Bloch or a Néel wall is the lowest energy state. Despite the fact that surface and volume magnetic charges are arranged in a two-dimensional (2D) fashion, overall the demagnetising energy can be considered as a transverse anisotropy which depends on the nanowire dimensions [18, 66]. A consequence of the model is that the azimuthal angle changes discontinuously as a function of the nanowire width and thickness [18, 68], contrary to our experimental findings. The possible existence of a "mixed wall" was discussed by Aharoni [6] in the context of in-plane magnetised films and discarded for the 1D case by a rigorous energy minimisation of all possible configurations. However, he conjectured that wall types with 2D spin arrangements with lower energy might exist, explaining, for instance, the occurrence of cross-tie walls [5].

5.5 Micromagnetic Simulations

To overcome the limitations of the 1D model, we performed 2D micromagnetic simulations. We used OOMMF [72] and mumax^3 [73] not only because the calculations of mumax^3 are running on the graphics processing unit of the computer and are therefore much faster than OOMMF which uses the central processing unit, but also in order to exclude errors. A wire with a length of 1200 nm and a width varying from 20 to 500 nm

was modelled with a cell size of 1 nm × 1 nm × 3.8 nm. The material parameters used were $K_u = 280\,\mathrm{kJ\,m^{-3}}$, $M_s = 570\,\mathrm{kA\,m^{-1}}$, and an exchange stiffness $A = 12\,\mathrm{pJ\,m^{-1}}$. For each of these simulations, the azimuthal angle was deduced from the relaxed energy state, see Figure 5.7. As expected, we found Néel walls for narrow wires and Bloch walls

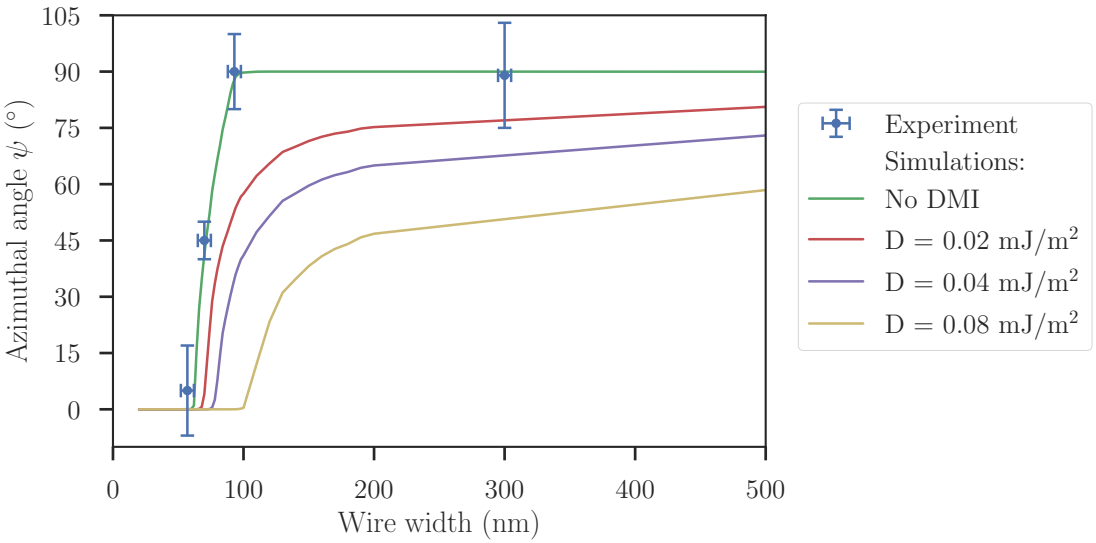

Figure 5.7: Azimuthal angle ψ versus nanowire width extracted from micromagnetic simulations. Without DMI, the domain wall type is Néel ($\psi = 0°$) for wires up to 60 nm, whereas for wires starting from 98 nm, the type is Bloch ($\psi = 90°$). In the transition region ψ changes continuously. By introducing DMI, Néel walls are stabilised, shifting the start of the transition towards wider wires and preventing pure Bloch walls even in 500-nm-wide wires. Our measured domain walls from Table 5.1 are included as data points.

for wide ones. The transition is not abrupt: ψ changes continuously between 60 nm and 98 nm, in agreement with our experimental findings. The width at which this transition occurs depends on the values of the material parameters: We find that for larger M_s or larger A the width gets larger, while for larger K_u it gets smaller.

In order to scrutinise the discrepancy between the analytical model and micromagnetic simulations, a series of 2D simulations was run for a wire of 70-nm width. A line of spins within the wall was kept fixed (sketch in inset in Figure 5.8), with the azimuthal angle varying from 0 to 90° in increments of 1°. The normalised energy of the system is plotted in Figure 5.8. For all spins fixed along the entire width, the lowest energy state is a Néel wall; no stable intermediate wall forms, despite the fact that the simulation is 2D. We then sequentially reduced the length of the line of fixed spins. In each series, starting from the edges, more spins were freed until in the extreme case only the spin in the centre cell was kept fixed. A pronounced energy minimum develops at a non-trivial angle, i.e., an intermediate wall has formed. This proves that the intermediate wall is a consequence of the 2D nature of a domain wall in perpendicularly magnetised wires.

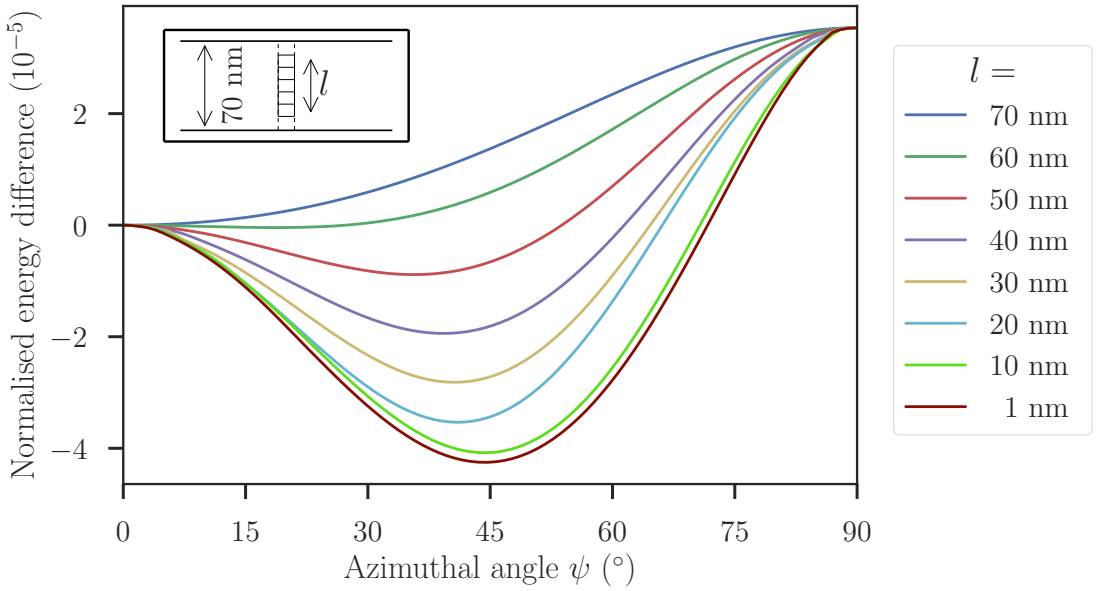

Figure 5.8: Normalised energy difference versus ψ for a 70-nm-wide wire. ψ was fixed along a line in the y-direction in the centre of the domain wall (inset) and varied between 0° and 90° in steps of 1°. The length l of the line of fixed spins varied from 70 nm (entire wire width) down to 1 nm (only cell at centre). The energy is plotted as the difference to the Néel wall and normalised by the energy of a single domain wire.

To highlight the difference energy contributions which are responsible for the lower energy state in the 2D case we plot the uniaxial anisotropy, exchange and demagnetisation energy versus the position along the y-direction. We extract the mean energy along the x-direction for a simulation with only the centre cell fixed (Figure 5.8 dark red line), subtract the mean energy of a simulation with only one cell in y-direction and normalise the difference to the mean energy of the whole wire with only one cell fixed. As shown in Figure 5.9 the uniaxial anisotropy and demagnetisation energy towards the wire's edges decreases while the exchange energy increases. This means the spins tend to align parallel to the edges in order to lower magnetostatic energy, similar to the formation of a Néel cap at the surface of a bulk ferromagnet [7], and contrary to a tilted 1D wall. In a perpendicularly magnetised ferromagnet, uniaxial anisotropy energy can be gained by tilting the spins within the wall out of the plane. In in-plane magnetised materials, such a tilting generally occurs by forming a C- or S-shaped spin arrangement [74], with a slight preference for the C-type because of the more complete flux closure of the stray field. Correspondingly, in our perpendicularly magnetised wire, a C-shaped arrangement is set up along the wire's cross section, as shown in Figure 5.10 (b). Within the wire plane, a C-shape cannot evolve into the adjacent up/down magnetisation in a continuous way, and hence an S-shape establishes itself, see Figure 5.10 (a), with an overall canting

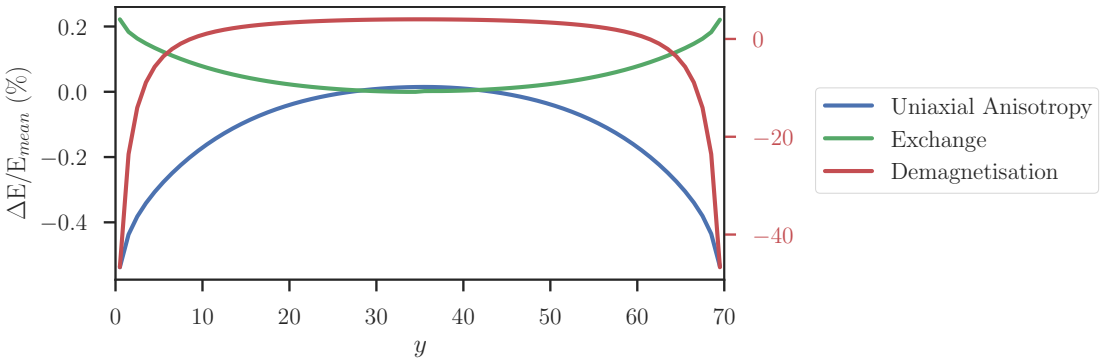

Figure 5.9: Difference in uniaxial anisotropy and exchange energy normalised to the mean energy. The demagnetisation energy uses the red scale on the right-hand side, while the uniaxial anisotropy and the exchange energy share the black scale on the left-hand side. For each y-position the mean energy along the x-direction was taken from a simulation where only the centre spin was fixed (Figure 5.8 dark red line) and the energy of a simulation with only one cell in y-direction (equivalent to the 1D model) was subtracted. The energy difference ΔE was then normalised to the mean energy E_{mean} of the simulation with the centre spin fixed.

angle of the wall of ≈3°. This inclination of the domain wall can also be seen in the measurements of Figure 5.5 (b)–(c). The contour levels in Figure 5.10 (a) reveal that the domain wall is slightly narrower at the edges than in the centre of the wire, illustrating that spins tilt out-of-plane, which reduces the uniaxial anisotropy energy near the edges. The azimuthal tilting of the spin within the wall is thus a consequence of the subtle interplay between anisotropy, exchange and demagnetising energy. The first tilts the spins out of the plane, while the second keeps neighbouring spins as aligned as possible. The third one balances the surface magnetic charges of the Bloch wall with the volume magnetic charges of a Néel wall. We suspect that an analogous situation exists in in-plane magnetised structures that are too small to support the wide extension of a cross-tie wall. Then the curved and tilted walls proposed long ago [1] might form.

So far, we neglected another mechanism that can strongly influence the structure of the domain wall: The Dzyaloshinskii–Moriya interaction [8, 9, 44, 63]. Strong DMI has been observed in asymmetric Co/Ni multilayers [75]. It influences the Bloch–Néel transition by expanding the Néel wall regime towards wider and thicker nanowires, so that in films the preferred domain wall will be of Néel type or Bloch type with a strong Néel component, i.e., a chiral intermediate wall.

In our wires, however, DMI is not the cause of the intermediate domain wall. First of all, we find Bloch walls in extended square structures and in the film (section 5.3). Second, from Table 5.1, we see that $\psi = (90 \pm 10)°$ in a 93-nm-wide nanowire and $\psi = (89 \pm 14)°$ in a 300-nm-wide one. Within the experimental uncertainty, these walls can be considered as Bloch walls with vanishing (or very small) Néel component. A Néel

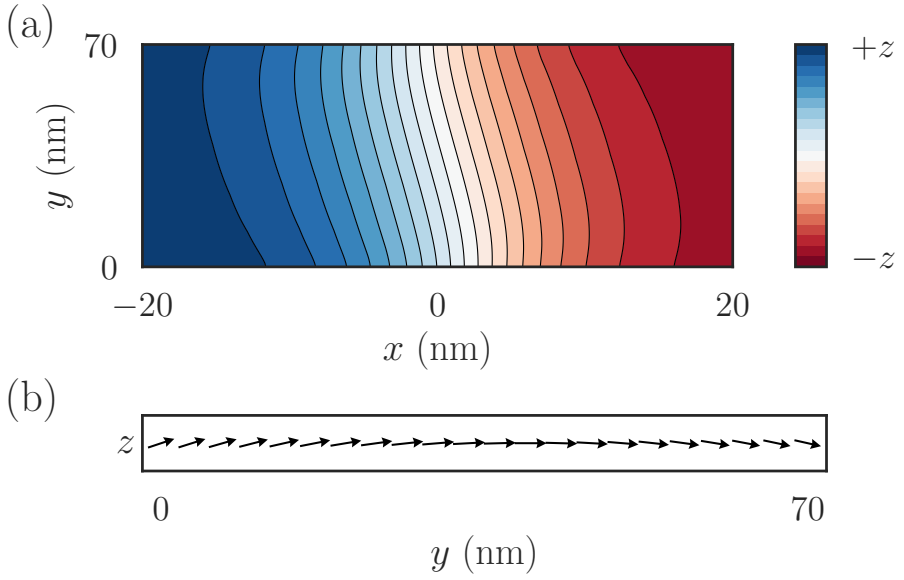

Figure 5.10: (a) Top view of a simulated intermediate domain wall in a 70-nm-wide perpendicularly magnetised wire. The out-of-plane component is indicated by colour graduation from blue ($+z$) to red ($-z$). The domain wall is slightly wider in the centre than at the edges of the wire. (b) Cross-section view at $x = 0$. The corresponding magnetisation direction is indicated with arrows. At the wire edges, a rotation of the z-component of the magnetisation is observed. It is opposite for opposite edges, leading to a slight canting and an S-shape appearance of the wall. Overall, the wall is inclined by $\approx 3°$ with respect to the wire's cross section. Since no chiral interaction is involved an inclination in the opposite direction is equally well possible, provided that the magnetisation tilt is also mirrored at the yz-plane.

component induced by DMI would be considerably more pronounced. To substantiate this, the micromagnetic simulations were repeated for wires with a DMI constant of $D = 0.04\,\mathrm{mJ\,m^{-2}}$, while keeping all other parameters the same. The results are shown in Figure 5.7. The striking difference is that ψ deviates strongly from 90° even at very large nanowire widths, for instance $\psi = 74°$ for a width of 500 nm. For the curve shown in Figure 5.7, we have deliberately chosen a very small value of D. The trend to favour a Néel wall component is even more pronounced for higher values of D, which is reported in material stacks similar to ours [75], until only chiral Néel walls are observed even in films. Therefore, we exclude that the intermediate walls we observe are caused by DMI.

5.6 Summary/Outlook

In conclusion, we determined the structure of domain walls as a function of the width of perpendicularly magnetised Co/Ni nanowires. Bloch walls prevail for wires wider

than 90 nm, Néel walls for wires narrower than 60 nm. The transition is not abrupt, contrary to expectations based on the commonly considered 1D model. We identified walls in which the magnetisation direction is intermediate between the two prototypical wall types. By micromagnetic simulations we showed that such a transition does not require additional effective transverse fields or DMI. The subtle balance of the various energy terms requires that the magnetisation configuration adopts a 2D distribution across the wire width. In particular, the spins within the wall tilt out of the plane when approaching the wire edge, in striking contrast to both a Bloch and a Néel wall. We argue that this intermediate wall type is a general phenomenon that should occur in any perpendicularly magnetised material provided the wire width is chosen appropriately. This width depends on the material parameters and can be tuned by the perpendicular anisotropy, saturation magnetisation, and exchange stiffness.

An overall inclination of the wall, which in our intermediate wall is a direct consequence of the magnetisation tilt, was observed in domain-wall motion experiments [76, 77]. It affects current-induced wall motion because of the induced wall pressure [78]. It was proposed that this inclination can be exploited to deduce the DMI value [79]. With our finding of an intermediate wall, one needs to carefully examine in each case whether such an inclination is caused by DMI alone or whether an achiral intermediate wall – unrelated to DMI – contributes.

It is remarkable that this new wall type has been overlooked for so long. In AMR measurements of wires which supposedly show the appearance of Bloch and Néel walls [66] we would also expect intermediate domain walls, provided the equilibrium state is attained. ψ of the walls could vary depending on pinning potentials, thus we would expect a normal distribution of the AMR in a histogram, not two distinct peaks for only Bloch and Néel walls as shown and interpreted in Ref. [66]. In micromagnetic simulations, the intermediate wall is missed if the starting configuration is a Bloch or a Néel wall, as for instance in Ref. [67]: The energy landscape is too flat there. Analytical approaches [68] captured the transition width accurately by developing sophisticated models for the magnetostatic energy, but were also unaware of the existence of a lower-energy 2D wall structure.

It would be interesting to investigate the consequences such continuous transition regions have on effects that rely on the discrete Bloch-to-Néel transition, such as the reported drastic reduction of the critical current in spin-transfer-driven domain wall motion [18] or the deferral of the Walker breakdown to higher fields [67].

6 Three-Dimensional Co Structures

Magnetic artificial spin ice systems can be used to simulate real frustrated systems, e.g., frozen water (water ice), and show interesting physics, e.g., "magnetic monopole defects" [80]. Magnetic artificial spin ices consist of highly ordered magnetic structures, e.g. square [81, 82] or kagome lattices (2D planar analogon of a honeycomb) [80, 83]. The order is chosen in such a way that at the conjunctions a frustrated magnetic state appears. We refer to "frustration" when a system has several states with the exact same energy, which leads to a non-trivial configuration. 2D artificial spin ice systems have been studied widely, 3D systems, however, were barely and only recently investigated.

In collaboration with the group of Sam Ladak from the School of Physics and Astronomy at the Cardiff University (Cardiff UK) we investigated 3D Co structures of different shapes and successfully imaged their magnetisation by spin-SEM. The idea is to combine these 3D structures (e.g., Figure 6.1) to create complex, extended magnetic networks, which then show frustration. Some results of this chapter are also used in a manuscript which was recently accepted for publication [84].

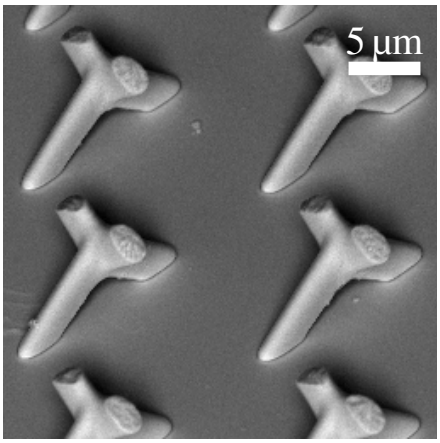

Figure 6.1: Array of early stage Co "tetrapods". The bottom two legs are connected to the substrate and make an angle of 30.5° with respect to it. At the vertex two more legs are placed with their long axis perpendicular to the one of the bottom ones, pointing upwards. The ellipsoidal cross-section of the wires is a consequence of TPL.

The samples were fabricated by combining two-photon lithography (TPL) with electrodeposition. The positive photoresist was spun onto a indium tin oxide (ITO)/glass substrate. TPL was then used to expose a 3D pattern within the resist. By immers-

ing the sample into a developer the exposed parts get removed, leaving behind hollow cavities in the shape of the desired structures. The resist acts as "mould" in the electrodeposition process, which fills the cavities with Co. Removing the rest of the resist yields then 3D Co structures [84]. We started with simple structures, i.e. pillars, and then worked towards tetrapod-like structures, with two wires (or "legs") up in the air and two legs connected to the substrate, making an angle of 30.5° with respect to it.

6.1 Multi-Domain State in Nano Pillars

Not only for the ease of fabrication but also for the imaging process it was favourable to start with simple structures: To our knowledge no one before has ever imaged 3D structures created by TPL with spin-SEM. We investigated samples consisting of arrays of pillars with different diameter. Prior to imaging we used sputter removal to clean the samples from C and O, which typically accumulate when exposed to air. In order to check the effect of the sputtering we could not employ Auger electron microscopy, because the area covered by the small 3D structures was negligible compared to the whole scanning area, thus the Auger spectrum only showed peaks from the substrate. Therefore we had to measure the structures in the spin-SEM without knowing the material composition of their surface.

A Co pillar with a diameter of 1.6 µm at the top is shown in Figure 6.2. The meas-

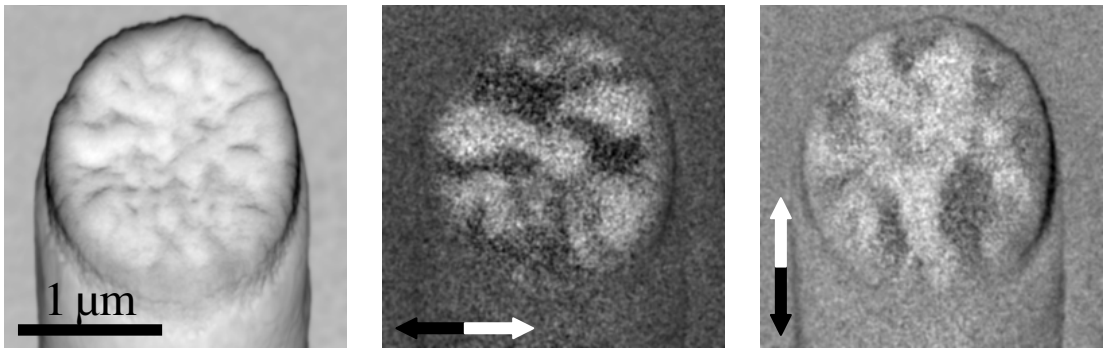

Figure 6.2: A Co pillar with a diameter of 1.8 µm at the top. The contrast in the magnetisation components is 8.5 %, indicating a well cleaned surface. The in-plane magnetisation pattern shows a randomly distributed multi-domain state.

urement was taken after exposure to an ion dose of $186\,\mathrm{C\,m^{-2}}$, which is necessary to clean the top surface thoroughly from resist. During acquisition the side walls of the pillars change their shape. We attribute this unusual behaviour to remaining quantities of resist being exposed by the electron beam of the spin-SEM. Even a long lift-off process and intense plasma etching after the electroplating did not completely remove the resist. The resist prevents magnetic imaging of the side walls, since sputter cleaning was not possible there because of geometrical restrictions. The in-plane magnetisation pattern at the top surface reveals a multi-domain state. A magnetisation along the long axis of

the pillar in the bulk can not be excluded by this measurement since flux closure at the top would also lead to an in-plane magnetisation as for example shown for Bloch domain walls in in-plane magnetised $Ni_{80}Fe_{20}$ [7]. However, measurements of a pillar lying on the ITO reveal also magnetic domains at the pillar's side wall, as shown in Figure 6.3. The magnetic contrast in the measurement of Figure 6.2 is 8.5 %, former measurements of a clean, flat, in-situ grown Co surface in our set-up show values of 15 % [85] while a Co film grown by electroplating shows 12 %. The discrepancy of the two films is most likely related to the electroplating process itself, which does not allow such a high purity Co as in-situ evaporation. The even lower contrast of the 3D pillars is probably related to the resist, which potentially influences the Co during the growing process.

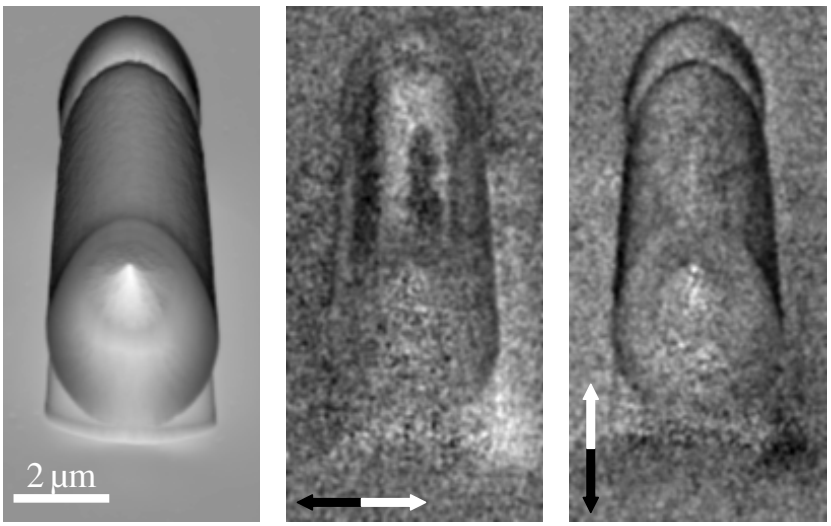

Figure 6.3: A Co pillar with a diameter of 3.5 µm which lies horizontally on the ITO substrate. The magnetisation is clearly not along the pillar's long axis, as revealed by the multi-domain state in the in-plane magnetisation component.

6.2 Multi-Domain State in Tetrapods

By reducing the dimensions of the structures tetrapods get more interesting since at the vertex, the position where the four wires meet, a frustrated state could emerge from single-domain wires magnetised along the long axis. We imaged tetrapods similar to the ones shown in Figure 6.1, but with a significantly reduced feature size. The wires had an elliptical cross-section with major and minor semiaxes of 0.89 µm and 0.66 µm, respectively, and a length of 8 µm. The tedrapods were arranged in arrays of 300 µm × 300 µm. The chemical composition was checked by energy dispersive x-ray analysis: The structures consisted of 95.4 % Co, 4.25 % C and 0.26 % O. The sample was first sputtered with the top sputter gun, whose ions hit the sample under 20° with respect to the sample surface, thus cleaning also the sides of the tetrapods. During the sputtering

process the sample was rotated three times by 90° at equidistant time steps, in order to clean all sides equally. This procedure exposes the tetrapods to an estimated ion dose of $16\,\mathrm{C\,mm^{-2}}$. Additionally the sample was sputtered with the focused sputter gun, which results in an additional ion dose of $20\,\mathrm{C\,mm^{-2}}$. A measurement of the area close to the vertex is shown in Figure 6.4. Magnetic contrast is observed only at the top surfaces of

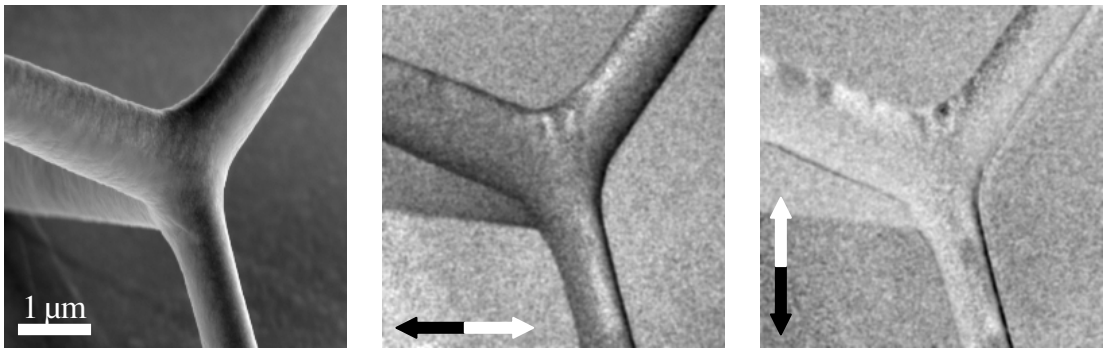

Figure 6.4: Topography and spin-polarised micrographs of a tetrapod. Prior the imaging the tetrapod was exposed to an ion dose of $36\,\mathrm{C\,mm^{-2}}$. The magnetisation components reveal multi-domain states in the vertex and legs, with a magnetic contrast of 3.5 %. In the x-component a few 180° domain walls can be observed, which seem to be characteristic for the vertex area.

the tetrapod. The tetrapod is in a multi-domain state in the vertex as well as in the wires. At the vertex several 180° domain walls can be observed in the x-component of the magnetisation. After applying a perpendicular magnetic field of $220\,\mathrm{kA\,m^{-1}}$ a new set of 180° walls forms at the vertex. Therefore we conclude that this magnetisation configuration is characteristic at the vertex of tetrapods of this size. The multi-domain state in the legs shows that also here the magnetisation is not pointing along the long axis, similar to the 3D pillars.

6.3 Challenges

As already mentioned in section 6.1, remaining resist at the 3D structures made measuring the magnetisation components with spin-SEM challenging. However, we were able to mitigate this with different approaches.

6.3.1 Top Surface Cleaning by Sputtering

For an array of pillars the ideal mould consists of homogeneously flat resist with holes in the shape of cylinders. The shape of the pillars is defined by the substrate at the bottom and the resist at the side. At the top, however, no boundary exists, making it susceptible to the growing conditions. For example the Co can grow out of the holes, creating randomly shaped tops. For measurements in our spin-SEM a flat surface is

ideal, because then the number of secondary electrons reaching the Mott detector will be highest, the magnetic contrast will not be influenced by topographic changes and the sputter cleaning process will be homogeneous. The sputter yield is a function of the incident beam angle. The angle for maximum sputter yield depends on the material to be sputtered and the inert gas, e.g., for Cu the angle for the maximum rate is around 60° for xenon (Xe) and 70° for neon (Ne) as sputter gas [86]. Thus on a curved sample the sputter process increased the curvature, making it more difficult to clean uniformly. Our investigations reveal different kind of surfaces at the top of the pillars as shown in Figure 6.5 (a)–(c). We also demonstrated the effect of intense sputtering of a curved

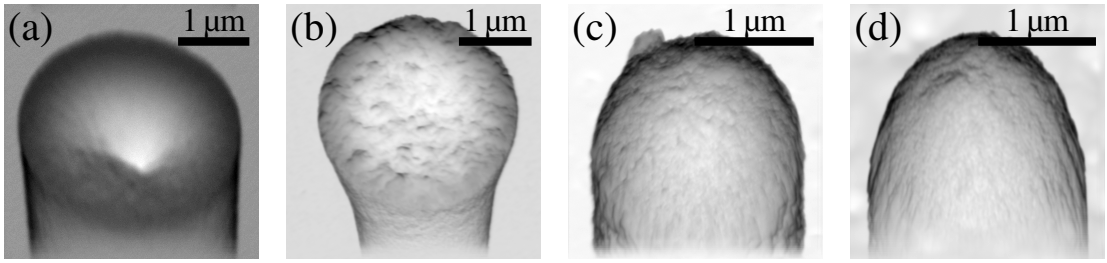

Figure 6.5: Micrographs of Co pillars of different size showing the different kind of surfaces. (c) and (d) show pillars of the same size before and after sputtering (ion dose of $1.7\,\mathrm{kC\,m^{-2}}$), respectively.

surface, as shown in Figure 6.5 (c) (before) and (d) (after). It leads, as expected, to a significant increase in the curvature. The magnetisation components of measurements Figure 6.5 (a)–(d) reveal, first, that in the case of (d) the sputtering did not improve significantly the magnetic contrast, second, that indeed a flat surface - as in (b) - yields the best magnetic contrast, as for example shown in Figure 6.2.

6.3.2 Cutting with Focused Ion Beam

By using a focused ion beam (FIB) to cut off the top of the pillars we were able to create a flat and clean surface. Due to possible implanting of gallium (Ga) atoms by the FIB and exposure to air during the transfer, the sample was mildly sputter cleaned before measuring in the spin-SEM. After a ion dose of $10\,\mathrm{C\,m^{-2}}$ (1 kV, 3.0 mPa, ×10, 5 min), a weak magnetic contrast was measurable, after additional 20 min, respectively $40\,\mathrm{C\,m^{-2}}$, a contrast of 4.5 % was measured (Figure 6.6). The weak contrast here is noteworthy since we basically measure the inside of the pillar, where the Co should be as pure as the growing process allows it. However, we do not know if there are Ga atoms left and how strong their influence on the magnetic contrast would be. Note also that the pillar is on the same sample and of the same size as the one shown in Figure 6.5 (c) and (d). The in-plane magnetisation components show a multi-domain state. In the absorbed current micrograph a $\approx 200\,\mathrm{nm}$ shell is revealed. The different contrast of shell and core shows that the shell has to be another material than Co. This is also confirmed by the missing magnetisation component for this area in the spin-polarised micrographs. We

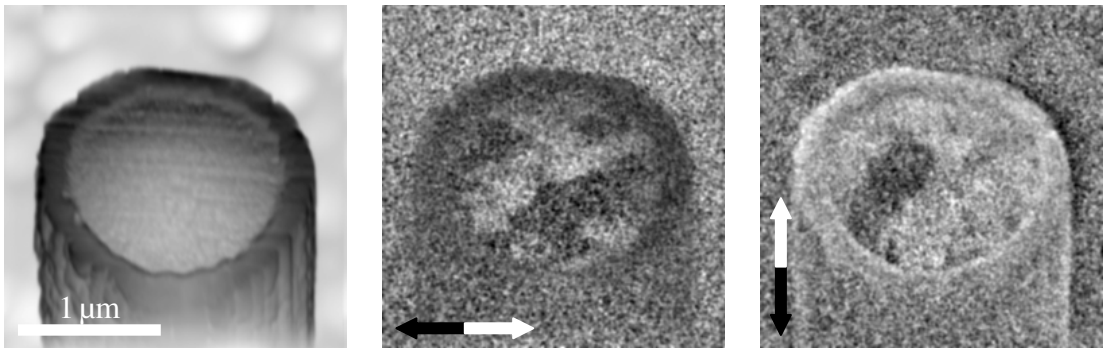

Figure 6.6: A pillar of the same size and from the same sample as the one in Figure 6.5 (d), but with top removed by FIB, guaranteeing a plane surface. After cleaning the sample with an ion dose of $50\,\mathrm{C\,m^{-2}}$, reasonable magnetic contrast is observed. The image on the left hand side shows the topography, a thick shell of a different material than Co is identified.

can exclude oxidisation as source, since for Co spontaneous passivation would stop the oxidation process after a view nanometres. Thus it must be leftovers of the photoresist.

6.3.3 Growing Process

All measurements were an important feedback for the growing process, which was steadily developed further by our collaborators in Cardiff. For example a longer lift-off and plasma etching process helped reduce the amount of leftover resist, which in turn enhanced the quality of the structures and measurements.

6.4 Summary

We successfully demonstrated that spin-SEM is able to measure 3D structures created by TPL in combination with electrodeposition. The tetrapod structures show already interesting magnetic features, e.g., the 180° domain walls at the vertex. In the future the investigation of smaller structures, which have their easy-axis along the wire long axis, will be the first step towards investigation of 3D, complex, extended magnetic networks, which show frustration.

The preferred magnetisation direction in wires is an interplay of shape and uniaxial magnetocrystalline anisotropy. In Co wires of size similar to ours the Co grows in grains of fcc and hexagonal close-packed (hcp) phase, however, literature does not agree on which is the preferred one [87, 88]. The hcp phase exhibits a uniaxial magnetocrystalline anisotropy directed along its hexagonal symmetry axis (c-axis). However, there is also no agreement on the orientation of the c-axis [88, 89]. This makes it hard to predict the strength and direction of the uniaxial magnetocrystalline anisotropy. At least in our wires spin-SEM and magneto-optical Kerr effect taken in Cardiff [84] measurements

reveal that it is not along the long axis.

This leads to two different approaches to force an easy axis along the wire long axis. One possibility would be to lower the feature size of the structures, therefore increase shape anisotropy. However this is limited by TPL, i.e. the set-up in Cardiff has a minimum feature size of approximately 280 nm [84]. It would be possible to lower the feature size by additional techniques, e.g. FIB or sputter removal. This approach would be useful for a first demonstration in tetrapods, however it would be not practical for extended networks and would not be a demonstration of the capabilities of TPL. Another approach would be to use magnetic materials which have a very low uniaxial magnetocrystalline anisotropy, i.e. $Ni_{80}Fe_{20}$. In this case the structures do not have to be as small as for Co, in order for the shape anisotropy to play the dominant role, forcing the magnetisation along the wire long axis.

Additionally, independent of the magnetisation direction in the structures, well controlled growing conditions and a thoroughly removal of the resist potentially will lead to substantially improved spin-polarised micrographs.

7 Conclusion and Outlook

In this thesis we exploited the unique feature of spin-polarised scanning electron microscopy: Direct probing of the magnetisation with high spatial resolution of 10 nm by analysing the spin polarisation of the secondary electron beam. In order to fully utilise this technique we constructed a spin rotator and implemented it in the system, which allowed us to measure all vector components of the magnetisation. The specimens were prepared in-situ to guarantee best possible cleanliness of the surface. We then not only studied magnetic domain formation in 3D structures on the micrometre scale but also domain walls on the nanometre scale, as has been demonstrated in three chapters:

Domains and domain walls have been studied in Fe and Ni on top of Cu(100). The material thickness was chosen such that the systems exhibit perpendicular magnetisation. From the presence of chiral Néel and intermediate walls we were able to identify DMI in these systems, which causes a right-handed chirality independent of the material combination we investigated. The sign as well as the absolute value were different from earlier measurements in a similar system [44], which suggested a DMI created at interfaces. Additionally we found intermediate domain walls even at large Ni thicknesses, which could be an indication of volume DMI. Possibly a symmetry breaking induced by releasing stress and/or misfit dislocations contributes to the DMI in our samples.

In Co/Ni multilayer systems which we tuned to exhibit also perpendicular magnetisation and structured as nanostripes we investigated the domain wall type in dependence of the stripes' width. We found a transition from Bloch domain walls in 93-nm-wide wire and above to Néel walls in a 57-nm-wide wire. The transition takes place continuously via an intermediate wall, contrary to an abrupt transition as supposed by earlier works. We found that the transition can be modelled by micromagnetic simulations and analysed it in more detail. We argue that the transition can be found in perpendicularly magnetised materials independent of the material parameters. The wire width at which the transition takes place and its extent can be tuned by changing the material parameters.

Additionally, we investigated three-dimensional Co structures, which were created by two-photon lithography and electroplating. This method is a promising candidate for future studies on 3D artificial spin ice systems, since extended networks can be created. Imaging with spin-SEM helped to identify problems in the growing process and most importantly showed magnetic domain formation. We were able to show that a smaller feature size is essential in order to have only one magnetic domain in pillars or in the arms of the tetrapods.

We can think of future developments in all three of this fields. A "softer" magnetic material for the 3D structures, e.g., $Ni_{80}Fe_{20}$, would allow single domain structures probably even at the current lateral dimensions. First samples of stacked $Ni_{80}Fe_{20}$ grids are

ready to be investigated and a first step in this direction. The Bloch to Néel wall transition via an intermediate wall shows that the current established theoretical models are inadequately to describe nano-magnetism in full detail. New models would help to even better understand the transition and probably also to find a way to explore intermediate domain walls for possible use in applications. The origin of chiral domain walls in differently arranged Ni and Fe on top of Cu(100) is not clear. Modifying the interface with heavy atom materials or other ferromagnetic materials could help to resolve this puzzle. Probably artificial control of the stress, i.e., by using a piezoelectric crystal as substrate, could give more insight into these systems. Additionally, theoretical calculations of strain induced DMI for fcc Fe or Ni on top of Cu(100) could probably solve the question where the DMI originates.

Bibliography

1. S. Shtrikman, D. Treves, *J. Appl. Phys.* **31**, 1304–1304 (1960).
2. I. Dzyaloshinsky, *J. Phys. Chem. Solids* **4**, 241–255 (1958).
3. T. Moriya, *Phys. Rev.* **120**, 91–98 (1960).
4. S. Methfessel, S. Middelhoek, H. Thomas, *J. Appl. Phys.* **31**, S302–S304 (1960).
5. E. J. Torok, A. L. Olson, H. N. Oredson, *J. Appl. Phys.* **36**, 1394 (1965).
6. A. Aharoni, *J. Appl. Phys.* **37**, 3271 (1966).
7. M. R. Scheinfein, J. Unguris, R. J. Celotta, D. T. Pierce, *Phys. Rev. Lett.* **63**, 668–671 (1989).
8. M. Heide, G. Bihlmayer, S. Blügel, *Phys. Rev. B* **78**, 140403(R) (2008).
9. A. Thiaville, S. Rohart, É. Jué, V. Cros, A. Fert, *EPL* **100**, 57002 (2012).
10. N. Perez, E. Martinez, L. Torres, S.-H. Woo, S. Emori, G. S. D. Beach, *Appl. Phys. Lett.* **104**, 092403 (2014).
11. G. Chen, A. T. N'Diaye, S. P. Kang, H. Y. Kwon, C. Won, Y. Wu, Z. Q. Qiu, A. K. Schmid, *Nat. Commun.* **6**, 6598 (2015).
12. Y. Yoshimura, K.-J. Kim, T. Taniguchi, T. Tono, K. Ueda, R. Hiramatsu, T. Moriyama, K. Yamada, Y. Nakatani, T. Ono, *Nat. Phys.* **12**, 157–161 (2015).
13. J. Kessler, *Polarized Electrons* (Springer, Berlin, 1976).
14. A. Crépieux, C. Lacroix, *J. Magn. Magn. Mater.* **182**, 341–349 (1998).
15. K. V. Shanavas, Z. S. Popović, S. Satpathy, *Phys. Rev. B* **90**, 165108 (2014).
16. J. M. D. Coey, *Magnetism and Magnetic Materials* (Cambridge University Press, Cambridge, 2010).
17. S. Tarasenko, A. Stankiewicz, V. Tarasenko, J. Ferré, *J. Magn. Magn. Mater.* **189**, 19–24 (1998).
18. S.-W. Jung, W. Kim, T.-D. Lee, K.-J. Lee, H.-W. Lee, *Appl. Phys. Lett.* **92**, 202508 (2008).
19. L. Néel, R. Pauthenet, *C. R. Acad. Sci.* **234**, 2172–2174 (1952).
20. A. Borovik-Romanov, M. Orlova, *Zh. Eksp. Teor. Fiz.* **31**, 579–582 (1956).
21. A. N. Bogdanov, U. K. Rößler, *Phys. Rev. Lett.* **87**, 037203 (2001).
22. P. Beck, M. Fähnle, *J. Magn. Magn. Mater.* **322**, 3701–3703 (2010).
23. A. Fert, P. M. Levy, *Phys. Rev. Lett.* **44**, 1538–1541 (1980).

24. S. Rohart, A. Thiaville, *Phys. Rev. B* **88**, 184422 (2013).
25. Z. Málek, V. Kamberský, *Czech. J. Phys.* **8**, 416–421 (1958).
26. B. Kaplan, G. Gehring, *J. Magn. Magn. Mater.* **128**, 111–116 (1993).
27. M. Speckmann, H. P. Oepen, H. Ibach, *Phys. Rev. Lett.* **75**, 2035–2038 (1995).
28. M. Knoll, E. Ruska, *Z. Phys.* **78**, 318–339 (1932).
29. E. Ruska, *Z. Phys.* **83**, 492–497 (1933).
30. C. Oatley, W. Nixon, R. Pease, in *Advances in Electronics and Electron Physics* (Elsevier, 1966), vol. 21, pp. 181–247.
31. N. F. Mott, *Proc. R. Soc. A* **124**, 425–442 (1929).
32. K. Koike, K. Hayakawa, *Jpn. J. Appl. Phys.* **23**, L187–L188 (1984).
33. K. Koike, H. Matsuyama, H. Todokoro, K. Hayakawa, *Jpn. J. Appl. Phys.* **24**, 1078–1081 (1985).
34. J. Unguris, G. G. Hembree, R. J. Celotta, D. T. Pierce, *J. Microsc.* **139**, RP1–RP2 (1985).
35. J. Stöhr, H. C. Siegmann, *Magnetism: From Fundamentals to Nanoscale Dynamics* (Springer, Berlin ; New York, 2006).
36. R. Allenspach, *IBM J. Res. Develop.* **44**, 553–570 (2000).
37. T. J. Gay, F. B. Dunning, *Rev. Sci. Instrum.* **63**, 1635 (1992).
38. T. J. Gay, M. A. Khakoo, J. A. Brand, J. E. Furst, W. V. Meyer, W. M. K. P. Wijayaratna, F. B. Dunning, *Rev. Sci. Instrum.* **63**, 114 (1992).
39. G. C. Burnett, T. J. Monroe, F. B. Dunning, *Rev. Sci. Instrum.* **65**, 1893 (1994).
40. T. Kohashi, H. Matsuyama, K. Koike, *Rev. Sci. Instrum.* **66**, 5537 (1995).
41. T. Kohashi, M. Konoto, K. Koike, *Rev. Sci. Instrum.* **75**, 2003 (2004).
42. T. Kohashi, M. Konoto, K. Koike, *J. Electron Microsc. (Tokyo)* **59**, 43–52 (2009).
43. D. A. Dahl, *Int. J. Mass Spectrom.* **200**, 3–25 (2000).
44. G. Chen, J. Zhu, A. Quesada, J. Li, A. T. N'Diaye, Y. Huo, T. P. Ma, Y. Chen, H. Y. Kwon, C. Won, Z. Q. Qiu, A. K. Schmid, Y. Z. Wu, *Phys. Rev. Lett.* **110**, 177204 (2013).
45. W. Platow, A. N. Anisimov, M. Farle, K. Baberscheke, *Phys. Status Solidi A* **173**, 145–151 (1999).
46. F. Huang, M. T. Kief, G. J. Mankey, R. F. Willis, *Phys. Rev. B* **49**, 3962–3971 (1994).
47. B. Schulz, K. Baberschke, *Phys. Rev. B* **50**, 13467–13471 (1994).
48. C. Klein, R. Ramchal, A. K. Schmid, M. Farle, *Phys. Rev. B* **75**, 193405 (2007).
49. M. Farle, W. Platow, A. N. Anisimov, P. Poulopoulos, K. Baberschke, *Phys. Rev. B* **56**, 5100–5103 (1997).

50. W. Platow, U. Bovensiepen, P. Poulopoulos, M. Farle, K. Baberschke, L. Hammer, S. Walter, S. Müller, K. Heinz, *Phys. Rev. B* **59**, 12641–12646 (1999).
51. M. Farle, *Rep. Prog. Phys.* **61**, 755–826 (1998).
52. J. Matthews, J. Crawford, *Thin Solid Films* **5**, 187–198 (1970).
53. G. Bochi, C. A. Ballentine, H. E. Inglefield, C. V. Thompson, R. C. O'Handley, H. J. Hug, B. Stiefel, A. Moser, H.-J. Güntherodt, *Phys. Rev. B* **52**, 7311–7321 (1995).
54. S. Müller, B. Schulz, G. Kostka, M. Farle, K. Heinz, K. Baberschke, *Surf. Sci.* **364**, 235–241 (1996).
55. M. Kronseder, T. N. G. Meier, M. Zimmermann, M. Buchner, M. Vogel, C. H. Back, *Nat. Commun.* **6**, 6832 (2015).
56. P. Talagala, P. S. Fodor, D. Haddad, R. Naik, L. E. Wenger, P. P. Vaishnava, V. M. Naik, *Phys. Rev. B* **66**, 144426 (2002).
57. D. S. Rodbell, *J. Appl. Phys.* **30**, S187–S188 (1959).
58. G. Wedler, H. Schneck, *Thin Solid Films* **47**, 147–153 (1977).
59. P. Srivastava, F. Wilhelm, A. Ney, M. Farle, H. Wende, N. Haack, G. Ceballos, K. Baberschke, *Phys. Rev. B* **58**, 5701–5706 (1998).
60. J. H. Dunn, D. Arvanitis, N. Mårtensson, *Phys. Rev. B* **54**, R11157–R11160 (1996).
61. T. N. G. Meier, M. Kronseder, C. H. Back, *Phys. Rev. B* **96**, 144408 (2017).
62. S.-G. Je, D.-H. Kim, S.-C. Yoo, B.-C. Min, K.-J. Lee, S.-B. Choe, *Phys. Rev. B* **88**, 214401 (2013).
63. A. Hrabec, N. A. Porter, A. Wells, M. J. Benitez, G. Burnell, S. McVitie, D. McGrouther, T. A. Moore, C. H. Marrows, *Phys. Rev. B* **90**, 020402(R) (2014).
64. K. Rivkin, K. Romanov, Y. Adamov, A. Abanov, V. Pokrovsky, W. M. Saslow, *EPL* **85**, 57006 (2009).
65. P.-O. Jubert, R. Allenspach, *J. Magn. Magn. Mater.* **290-291**, 758–760 (2005).
66. T. Koyama, D. Chiba, K. Ueda, K. Kondou, H. Tanigawa, S. Fukami, T. Suzuki, N. Ohshima, N. Ishiwata, Y. Nakatani, K. Kobayashi, T. Ono, *Nat. Mater.* **10**, 194–197 (2011).
67. E. Martinez, L. Torres, L. Lopez-Diaz, *Phys. Rev. B* **83**, 174444 (2011).
68. M. D. DeJong, K. L. Livesey, *Phys. Rev. B* **92**, 214420 (2015).
69. S. Meckler, N. Mikuszeit, A. Preßler, E. Y. Vedmedenko, O. Pietzsch, R. Wiesendanger, *Phys. Rev. Lett.* **103**, 157201 (2009).
70. J.-P. Tetienne, T. Hingant, L. Martínez, S. Rohart, A. Thiaville, L. H. Diez, K. Garcia, J.-P. Adam, J.-V. Kim, J.-F. Roch, I. Miron, G. Gaudin, L. Vila, B. Ocker, D. Ravelosona, V. Jacques, *Nat. Commun.* **6**, 6733 (2015).

71. B. Boehm, A. Bisig, A. Bischof, G. Stefanou, B. J. Hickey, R. Allenspach, *Phys. Rev. B* **95**, 180406(R) (2017).

72. M. J. Donahue, D. Porter, 'OOMMF User's Guide, Version 1.0', 6376 (National Institute of Standards and Technology, Gaithersburg, MD, 1999).

73. A. Vansteenkiste, J. Leliaert, M. Dvornik, M. Helsen, F. Garcia-Sanchez, B. Van Waeyenberge, *AIP Adv.* **4**, 107133 (2014).

74. K. Y. Guslienko, V. Novosad, Y. Otani, H. Shima, K. Fukamichi, *Phys. Rev. B* **65**, 024414 (2001).

75. G. Chen, T. Ma, A. T. N'Diaye, H. Kwon, C. Won, Y. Wu, A. K. Schmid, *Nat. Commun.* **4**, 2671 (2013).

76. M. Yamanouchi, D. Chiba, F. Matsukura, T. Dietl, H. Ohno, *Phys. Rev. Lett.* **96**, 096601 (2006).

77. K.-S. Ryu, L. Thomas, S.-H. Yang, S. S. P. Parkin, *Appl. Phys. Express* **5**, 093006 (2012).

78. M. Viret, A. Vanhaverbeke, F. Ott, J.-F. Jacquinot, *Phys. Rev. B* **72**, 140403(R) (2005).

79. O. Boulle, S. Rohart, L. D. Buda-Prejbeanu, É. Jué, I. M. Miron, S. Pizzini, J. Vogel, G. Gaudin, A. Thiaville, *Phys. Rev. Lett.* **111**, 217203 (2013).

80. S. Ladak, D. E. Read, G. K. Perkins, L. F. Cohen, W. R. Branford, *Nat. Phys.* **6**, 359–363 (2010).

81. R. F. Wang, C. Nisoli, R. S. Freitas, J. Li, W. McConville, B. J. Cooley, M. S. Lund, N. Samarth, C. Leighton, V. H. Crespi, P. Schiffer, *Nature* **439**, 303–306 (2006).

82. J. P. Morgan, A. Stein, S. Langridge, C. H. Marrows, *Nat. Phys.* **7**, 75–79 (2011).

83. G. Möller, R. Moessner, *Phys. Rev. B* **80**, 140409(R) (2009).

84. G. Williams, M. Hunt, B. Boehm, A. May, M. Taverne, D. Ho, S. Giblin, D. Read, J. Rarity, R. Allenspach, S. Ladak, *Nano Res.* (2017).

85. R. Allenspach, M. Stampanoni, A. Bischof, *Phys. Rev. Lett.* **65**, 3344–3347 (1990).

86. A. W. Czanderna, Ed., *Methods of Surface Analysis* (Elsevier Scientific Pub. Co, Amsterdam ; New York, 1975).

87. Z. Ye, H. Liu, Z. Luo, H.-G. Lee, W. Wu, D. G. Naugle, I. Lyuksyutov, *Nanotechnology* **20**, 045704 (2009).

88. K. R. Pirota, F. Béron, D. Zanchet, T. C. R. Rocha, D. Navas, J. Torrejón, M. Vazquez, M. Knobel, *J. Appl. Phys.* **109**, 083919 (2011).

89. Y. Henry, K. Ounadjela, L. Piraux, S. Dubois, J.-M. George, J.-L. Duvail, *Eur. Phys. J. B* **20**, 35–54 (2001).